Accepted for publication in Int. J. Heat Mass Transfer on 23 March 2021

Flow topology and bifurcations of buoyancy and mixed convection in an elongated channel with an abrupt section variation

Saad Inam and Marcello Lappa[1]

[1]Department of Mechanical and Aerospace Engineering, University of Strathclyde, James Weir Building, 75 Montrose Street, Glasgow, G1 1XJ, UK – email: marcello.lappa@strath.ac.uk

Abstract: A forward-facing step (FFS) located half-way in an elongated duct subjected to a horizontal pressure gradient and a vertical temperature difference is considered as a simplified geometrical model to investigate numerically typical problems of internal non-isothermal flow in the presence of blunt obstacles. The sensitivity of this system to thermal buoyancy for each considered rate of fluid injection (measured through the related Richardson number, *Ri*) is explored by varying parametrically the corresponding Rayleigh number (*Ra*) over a large interval of orders of magnitude (up to the onset of chaos) and assuming two alternate paradigms for the bottom of the considered channel, namely an adiabatic or kept-at-constant temperature (hot) boundary. Through this conceptual framework, a kaleidoscope of situations are revealed in the (*Ri*, *Ra*) space, differing in terms of flow patterning behavior, thermal plume generation phenomena, intensity of heat exchange at the walls and bifurcation scenario. In particular, while for the isothermal floor case a higher Ri leads to an increase in the value of the Rayleigh number needed for transition to time-dependent flow, the corresponding trend becomes non-monotonic if the same boundary is thermally insulated. In such a case the Nusselt number (Nu) calculated for the horizontal surface of the step is always smaller than the equivalent Nu evaluated for the vertical side. The latter is significantly lowered when the hot-floor condition is assumed.

Key words: Mixed forced/buoyancy flow, heat exchange, instability and bifurcation in fluid dynamics.

1. Introduction

Isothermal and non-isothermal problems involving fluid flow and related instabilities are widespread in engineering ([1-6]). In particular, fluid motion in channels or other similar confined geometries in the presence of one or more obstructions constitutes an archetypal subject that is of great relevance to many technological and industrial processes. This explains why an overwhelming amount of results can be found in the literature about fluid behavior inside hydraulic circuits of various types used in chemical plants or food-processing industries. These pipe systems often display sudden changes in the cross-sectional area and/or ribs and baffles may be present, which are mounted in a direction perpendicular to the prevailing current. These geometrical features can significantly disturb the regular motion of the fluid and produce vorticity eddies or other types of (steady or oscillatory) disturbances (Molochnikov et al., [7]). Similar problems also affect the very general area of fluid machinery; indeed, in many situations connected with this specific field, flow

separation can produce an undesired increase in the frictional shear stress leading to significant energy losses (Hattori and Nagano [8]). A flow disturbed by localized protuberances or other types of blockage is also a typical subject of analysis for engineers concerned with the design of ground vehicles using wind tunnels (Dai et al. [9]; Redchyts et al., [10]) or plants for the production of wind energy (Sherry et al. [11]).

These very common and relatively simple examples may be regarded as a justification for the great interest that the fundamental problem connected with the spatio-temporal behavior (*steady, oscillatory or turbulent*) of fluid motion in the presence of geometrical expansions, contractions or orifices has enjoyed over recent years.

In particular, a specific configuration on which many studies have concentrated is the so-called *forward-facing step* (FFS). This paradigm has specifically been introduced as a simplified workhorse to support the analysis of fundamental aspects linked to *the typical interaction of a flowing fluid with a blunt obstacle*. Relevant examples pertaining to this line of inquiry are Refs [11-18]; notably, these works have been instrumental in revealing that if a duct exhibits a shrinkage in the cross-sectional area, the resulting dynamics can become very involved (often these flows can display a variety of possible responses, for which all the possible underlying cause-and-effect relationships have not been clarified yet).

Interestingly, meaningful comparison with the companion "mirror" configuration (backward-facing step, BFS) has led over the years to the unexpected realization that the typical outcomes of the flow-step interaction tend to be more complex when the decrease of the cross-sectional area *occurs in the downstream direction* (FFS case, [19-21]). Whilst for the BFS, only one separated region is produced (downstream of the geometrical expansion), with the forward-facing step, disconnected regions of intense vorticity can be created (typically, one being located upstream and the other downstream from the step). The second region with significant vorticity originates from the leading edge (top of the vertical step wall) and extends in the downstream direction leading to the formation of a "bubble" [18]. As illustrated by several authors [22-24], specific dynamics originating from this localized region of recirculating fluid can produce unsteadiness and other complex outcomes.

Along these lines, some studies have shown that the emerging oscillatory or turbulent behavior can have a remarkable impact on the transport of chemical species and/or heat (Moosavi and Nassab [24]; Nassab et al. [25]; Oztop et al. [26], Xie and Xi [27]). It is also known that, in turn, these can take a much more active role and *exert a back influence on the flow*. This is especially true if a significant amount of *heat* is being exchanged between the fluid and the solid walls of the considered duct.

When the fluid is in non-isothermal conditions *mechanisms of buoyancy nature* start to play a role. Typically, while relatively cold fluid tends to fall down, warmer fluid moves in the opposite direction and this results in the formation of *vertical currents* or *thermal plumes*. In horizontal ducts, such currents or plumes can have an impact similar to that of obstacles mounted in a direction perpendicular to the wall (see, e.g., [28-33]). They can produce recirculation regions, which in turn can deeply influence the performance of many devices.

Evidence for such behaviors can be found in chemical and energy production plants, environmental control devices, heat exchangers of various types, cooling systems for electronic devices and nuclear reactors, combustion chambers and cooling passages in turbine blades, etc., see, e.g., Sun and Jaluria [34]; Arrif et al. [35]; Nadjib et al., [36]; Lappa [37]). All these technological problems consistently bare the presence of thermal buoyancy convection and related instabilities, which require a proper understanding of the underlying mechanisms.

A large cross section of fundamental research for the FFS problem can be found in Abu-Mulaweh et al. [22, 23] and Lappa and Inam [38]. These studies specifically concentrated on different ranges of the relevant control parameters. As an example, the former authors varied the Reynolds number and Grashof numbers (based on the step height) in the intervals, $O(10^2) \leq Re_h \leq O(10^3)$ and $O(10^3) \leq Gr_h \leq O(10^4)$). They illustrated that, on increasing the thickness of the step, the spatial extension of the recirculation regions grows while the heat transfer rate from the heated downstream displays the opposite behavior (moreover, both quantities become higher as the inlet velocity grows). They also reported that in some situations no upper recirculation area is formed, while in other circumstances the mechanism leading the system from laminar to turbulent originates just in this region.

Lappa and Inam [38] focused on a more compact geometry (a square cavity with a geometrically similar obstruction on the bottom) addressing a variety of cases stemming from different possible thermal boundary conditions for the floor of the cavity and the relative position of the inflow and outflow sections. These authors examined cases with the Rayleigh number (based on the cavity height) spanning the range $O(10^3) \leq Ra \leq O(10^8)$ and values of the Richardson number $Ri=\infty$ (pure buoyancy convection) and $Ri \cong 1$ (for which the relative importance of buoyancy and forces convection are the same).

Their study has revealed that, for pure buoyancy heat islands can be formed in the lower part of the domain as a result of the insufficient mixing between the upper and lower fluid regions that is established when the flow pattern takes a specific topological configuration (at relatively high values of Ra). For hybrid convection, a variety of other patterns were observed, corresponding to different possible realizations of the route that cold fluid can take to reach the outlet. These possible multiple paths were interpreted taking into account the rich variety of possible interactions that can be established between the cold fluid injected in the cavity and the buoyancy flow of thermal nature originating from the hot surfaces (the latter can support or oppose to the transport of fluid from the inflow to the outflow section depending on the considered conditions).

To the best of our knowledge, these are the only studies where the interplay of buoyancy and forced convection was intentionally investigated in FFS systems. However, partially relevant information can also be gathered from existing numerical studies about gravity-driven and hybrid buoyancy-Marangoni flow in crucibles with different shapes used for the production of semiconductor or opto-electronic materials (see, e.g., [39-42]) or other studies concerned with building heating and ventilation or electronic devices cooling (Sun and Jaluria [34]; Yarin [43]; Venkatasubbaiah and Jaluria [44]; Morsli et al. [45]; Kachi et al. [46]).

As the reader might have realized at this stage, with the exception of the above efforts, it stands out that there is a surprising lack of information about the effect of buoyancy on forced flow in partially obstructed channels. This knowledge shortage is essentially a consequence of the variety of factors potentially influencing the resulting flow and the complexity of the dynamics *per se*. While each of these factors on its own presents significant challenges to a full understanding of the physics controlling fluid behavior over a FFS, when combined they may give rise to novel and/or unexplored phenomena.

Motivated by this observational tide, in the present work we concentrate on such a problem in the framework of direct numerical simulation. In order to complement the earlier investigation by Lappa and Inam [38], where the analysis was limited to a compact (square) cavity with $Ri \cong 1$, here we consider an extended channel and a relatively wide range of values of the Richardson number, however, still allowing the Rayleigh number to span an extended set of orders of magnitude.

2. Mathematical and Numerical model

As this is the first time that specific problem related to hybrid forced-buoyancy convection is considered in an elongated duct with a forward-facing step (FFS) located half-way, we follow a standard practice, which has already enjoyed a widespread use in the literature, i.e. we consider this new problem in the simplified framework represented by a two-dimensional (2D) configuration. We wish to remark that, historically, the development of the companion problem represented by standard buoyancy convection in differentially heated cavities (heated form below or from the side) took a similar path essentially as a result of the declared intention of investigators to discern three-dimensional (3D) effects through comparison with simulations initially conducted under the constraint of two-dimensionality. The same concept also applies to earlier studies about forced (isothermal) convection for the forward-facing step (FFS) case. In the early stages of investigation of this problem, the simulations were carried out assuming the flow to be 2D. The present work should be seen as another example of such a practice or way of thinking (a “first step” along such a modeling/analysis hierarchy).

2.1 The Geometry and related boundary conditions

The considered physical domain is sketched in Fig. 1. It consists of a rectangular two-dimensional channel of transverse size d, and total length $L=10d$ formally divided in two parts of identical horizontal extension by a sudden change in the available cross-sectional area (due to the presence of a forward facing step having thickness equal to half of the channel height, i.e. $d/2$).

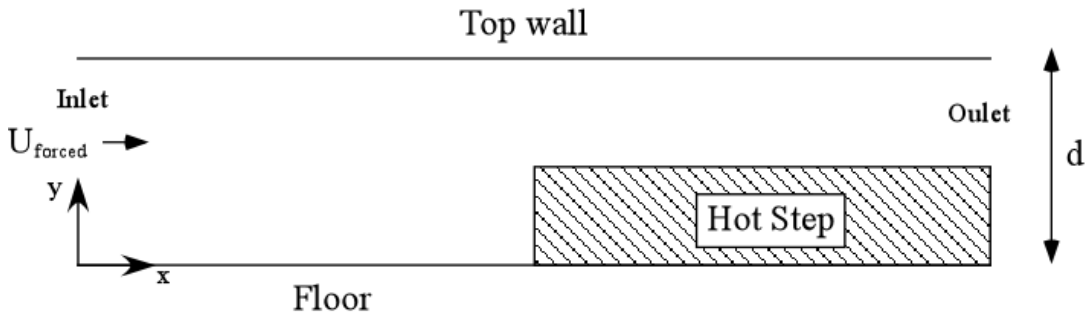

Figure 1: Sketch of the considered FFS geometry and related kinematic and thermal boundary conditions.

The top and bottom boundaries are solid and different thermal boundary conditions can be imposed for them. Here, the top wall is considered adiabatic for all cases with non-zero values of the Reynolds number, whereas it is assumed isothermal (at temperature T_{cold}) when the case of pure buoyancy convection is considered (i.e. Reynolds number Re=0, U_{forced} =0, for this case the left and right, inflow and outflow, sections are replaced by solid adiabatic walls). The situation with pure thermal convection is considered for the sake of completeness and to complement the earlier study by Lappa and Inam [38]. For Re≠0 the fluid injected into the channel is assumed to have initial temperature T_{cold}.

A separate discussion is needed for the floor and the step boundary (consisting of a small vertical segment and the horizontal boundary which extends from its corner in the downstream direction).

The floor is assumed either adiabatic or at constant temperature (set at the temperature T_{hot}). The entire boundary of the step is considered at temperature T_{hot} regardless of all the other thermal boundary conditions assumed for the top and bottom walls.

2.2 Governing equations and characteristic numbers

In order to make the outcomes of the present study more general, it is entirely formulated in terms of non-dimensional quantities. Accordingly, the following reference scales are used: α/d as velocity scale (where α is the fluid thermal diffusivity), and $\rho\alpha^2/d^2$ and d^2/α, as reference quantities for pressure and time (where ρ is the fluid density), respectively. With this approach, the non-dimensional equations for the balance of mass and momentum can be cast in compact form as:

$$\underline{\nabla}\cdot\underline{V}=0 \tag{1}$$

$$\frac{\partial \underline{V}}{\partial t}=-\underline{\nabla}p-\underline{\nabla}\cdot\left[\underline{V}\,\underline{V}\right]+\nabla^2\underline{V}-\mathrm{Pr}\,Ra T\;\underline{i}_g \tag{2}$$

where

$$Ra = \mathrm{Pr}\, Gr = \frac{g\beta_T \Delta T d^3}{\nu\alpha} \tag{3}$$

is the classical Rayleigh number. The parameter β_T appearing in its expression is the so-called fluid thermal expansion coefficient. From a formal point of view it follows from the so-called Boussinesq approximation by which the variations of density are linked to the corresponding changes of temperature through a linear relationship based on this parameter; moreover, ν is the kinematic viscosity of the considered fluid (the ratio ν/α being the well-known Prandtl number Pr, set to 1 in the present study). If the nondimensional temperature is defined as the ratio between the local temperature (after subtracting T_{cold}) and the imposed ΔT, a nondimensional version of the energy equation can be written as

$$\frac{\partial T}{\partial t} + \underline{\nabla} \cdot \left[\underline{V} T\right] = \nabla^2 T \tag{4}$$

The Reynolds number can be introduced on the basis of its classical definition, i.e.

$$\mathrm{Re} = \frac{U_{forced} d}{\nu} \tag{5}$$

Most conveniently, Re and *Ra* can be combined into a single nondimensional parameter, known as the *Richardson number*:

$$Ri = \frac{g\beta_T \Delta T d}{U_{forced}^2} = \frac{Ra}{\mathrm{Pr}\,\mathrm{Re}^2} \tag{6}$$

The advantages relating to the use of this group rest on the idea that it can be used to estimate 'a priori' the relative importance of buoyancy and forced convection (the two limit cases corresponding to *pure buoyancy convection* or *forced flow* being recovered in the limit as the Richardson number tends to *infinite* or *zero*, respectively).

Before starting to deal with the results, we wish to remark that, if the FFS geometry is considered, the former situation ($Ri \to \infty$, only buoyancy being present, i.e. Re=0) deserves some attention since, even in the absence of forced flow, two different convective mechanisms can compete in determining the emerging flow pattern. In a geometry with a heated step, these two mechanisms can coexist because the structure of buoyancy convection greatly depends on the *orientation of the hot surface generating it*. If the surface is horizontal (and therefore the prevailing temperature gradient is vertical), the emerging flow is known as Rayleigh-Bénard (RB) convection ([47]). If the surface is vertical (responsible for the emergence of a horizontal temperature difference), then the flow is generally referred to as "Hadley convection" (e.g., [48]).

Despite the similarities in terms of driving force and related processes, these two forms of thermal convection can display very different behaviors for what concerns their stability and transition to chaos (see, e.g., [49]). The presence of forced flow can obviously lead to a third independent convective process superimposed on those of purely buoyant nature. In the present study, we will therefore be addressing the triadic relationship among these three distinct mechanisms of convection.

2.3 Boundary conditions

By indicating with A the ratio L/d, the non-dimensional thermal boundary conditions for the FFS configuration can be summarized as follows:

$\underline{V}=0$ on all solid walls (7)

Step walls (x=A/2, 0≤y≤1/2 and y=1/2, A/2≤x≤A) $T=1$ (8)

Floor (y=0, 0≤x≤A/2), $\partial T/\partial y=0$ (adiabatic) (9a)
or $T=1$ (isothermal) (9b)

Top wall (y=1, 0≤x≤A) $T=0$ (isothermal, Re=0) or $\partial T/\partial y=0$ (adiabatic, Re≠0) (10)

A separate discussion is needed for the lateral boundaries located at x=0 and x=A. These boundaries are considered solid and adiabatic if no forced flow is considered, whereas, for Re≠0 the left and right boundaries are assumed to be inflow and outflow sections, respectively. Therefore:

For Re=0, $\partial T/\partial x=0$ at x=0 and x=A (11)

For Re≠0, x=0 (inflow, 0≤y≤1), $T=0$ and $u= U_{\text{forced}}$ (12)

x=A (outflow, 0.5≤y≤1): $\frac{\partial u}{\partial t}+D\frac{\partial u}{\partial x}=0$, $\frac{\partial v}{\partial t}+D\frac{\partial v}{\partial x}=0$, $\frac{\partial T}{\partial t}+D\frac{\partial T}{\partial x}=0$ (13)

Equation (13) is known as the "prognostic' equation (it is a "dynamic" boundary condition). The quantity D appearing there is a constant assumed to be equal to the averaged velocity perpendicular to the boundary $D=\underline{V}\cdot\underline{\hat{n}}$ (this special condition is needed to mitigate non-physical fluctuations in the velocity and temperature at the outlet; the interested reader being referred to the works by Hattori et al. [50]; Dong et al. [51] for additional details about this well-known numerical problem). Moreover, the Nusselt for the vertical and horizontal walls of the step is defined here as:

$$Nu_{step}^{vert} = -2\int_0^{1/2} \frac{\partial T}{\partial x} dy \text{ and } Nu_{step}^{horiz} = \frac{2}{A}\int_{A/2}^{1} \frac{\partial T}{\partial y} dx \tag{14}$$

2.4 The Numerical method

The set of equations (1), (2) and (4) and related boundary conditions have been solved numerically using the PISO (Pressure Implicit Split Operator) technique originally proposed by Issa [52]. This technique is available as an independent solver in the frame of the OpenFoam computational platform.

This method relies on the so-called Hodge decomposition theorem (see, e.g., [53]), i.e. on the possibility to split any vector field into a divergence-free contribution and the gradient of a scalar potential (a curl-free part). An important outcome of this theorem is that a velocity field can be considered fixed when its curl (vorticity) and divergence (and normal component at the boundary) are known. The implications of this theorem can be used to implement a time-marching procedure where velocity and pressure (which appear at the same time in the momentum equation) are computed in a partially segregated manner.

This modus operandi is at the basis of many techniques [54-58], generally known as projection or fractional-step methods. In practice, these methods take advantage of the mathematical property of any gradient of a scalar function to be annihilated when the curl operator is applied to the equation that contains it.

This apparently innocuous observation implies that if the momentum equation is simplified by removing $\underline{\nabla}p$, the resulting equation will produce a velocity field that features the same vorticity that would be possessed by the velocity field satisfying the original equation:

$$\frac{\partial \underline{V}^*}{\partial t} = \left[-\underline{\nabla}\cdot\left[\underline{V}\,\underline{V}\right] + \mathrm{Pr}\,\nabla^2 \underline{V} + \mathrm{Pr}\,Ra T \underline{i}\right] \tag{15}$$

This velocity field is generally called the "intermediate velocity" field $\underline{V}^*$. The asterisk is used to indicate that though it is physically consistent in terms of vorticity, however, it does not satisfy the incompressibility constraint mathematically represented by eq. (1).

The next stage of this decomposition hierarchy obviously calls for a step where the flow is made solenoidal, i.e. it is forced to satisfy eq. (1). This is typically achieved by reintroducing the previously neglected pressure gradient and expressing formally the velocity as

$$\underline{V} = \underline{V}^* - \xi \underline{\nabla} p \tag{16}$$

(where ξ is a constant generally set equal to the time integration step Δt). Taking the divergence of this expression and forcing it to be zero leads to another equation of elliptic nature (a Poisson equation):

$$\nabla^2 p = \frac{1}{\Delta t} \underline{\nabla} \cdot \underline{V}^* \tag{17}$$

These formal passages can be turned into an effective numerical procedure by using the above-mentioned Poisson equation to determine the pressure and then using eq. (16) to compute a final velocity field, which at the same time will be solenoidal (incompressible) and feature the correct amount of vorticity.

With OpenFoam such equations are numerically solved in the framework of a collocated grid approach, i.e. the center of the cells is used to store all the variables (while good coupling of velocity and pressure is supported through the adoption of a special interpolation scheme for the velocity on the cell faces [59]).

In addition to the above descriptions, we wish to highlight that in the present work both the convective and diffusive terms appearing in momentum and energy equations have been discretized using second order central difference schemes. The resulting system of algebraic equations has been treated using a Preconditioned Bi-Conjugate Gradient (PBiCG) with an Incomplete Lower Upper (DILU) preconditioner in the predictor step. A Generalized Geometric-Algebraic Multi-Grid (GAMG) method has finally been employed to determine the solution of eq. (17).

2.5 Algorithm Validation

In order to demonstrate the reliability of the algorithm described in Sect. 2.4 and its ability to address the problem set in the introduction, we have duly verified and validated it through comparison with available benchmarks and test cases. In particular, such a process has been articulated into three distinct stages of verification. Initially, two different archetypal settings have been considered, namely steady RB and Hadley convection in a square cavity (related validation results being summarized in Tables I and II, respectively).

Table I: A=1, Rayleigh-Bénard convection in a square cavity with adiabatic sidewalls, Ra=10^5, Pr=0.71. Comparison with Table 2 of Ouertatani et al. [60], uniform mesh 128x128. Velocity scaled with u_0=sqrt(gβ_THΔT).

Quantity	Present	Ouertatani et al. [60]
U_{max}	0.3443	0.3442
V_{max}	0.3754	0.3756
Nu_h	3.9204	3.9097

Table II: Hadley flow, $Ra=10^6$, Pr=0.71, square cavity with adiabatic top and bottom wall, uniform mesh 100x100 (Legend: $|\psi|_{max}$ - Maximum absolute value of the stream function, v_{max} - Max vertical velocity component on a horizontal mid-plane, x_{max} - Position of v_{max}, u_{max} - Max horizontal component on a vertical mid-plane, y_{max} - Position of u_{max}. Nu_{hot} - Average Nusselt number on the hot boundary. $Nu_{max,hot}$ - Maximum Nusselt number on the hot boundary, $y_{Nu,max}$ - Position of $Nu_{max,hot}$, $Nu_{min,hot}$ - Minimum Nusselt number on the hot boundary, $y_{Nu,min}$ - Position of $Nu_{min,hot}$).

Parameter	present	De Vahl Davis and Jones [61]
$\|\psi\|_{max}$	16.919	16.750
v_{max}	216.09	219.36
x_{max}	0.0368	0.0379
u_{max}	64.97	64.63
y_{max}	0.848	0.850
Nu_{hot}	8.913	8.817
$Nu_{max,hot}$	18.193	17.925
$y_{Nu,max}$	0.0368	0.0378
$Nu_{min,hot}$	0.970	0.989
$y_{Nu,min}$	1	1

As a second stage of validation, the ability of the present numerical approach *to capture properly the transition from steady to oscillatory flow* has been assessed (the outcomes of this dedicated study being summarized in Figs. 2 and Table III). This type of instability corresponds to the so-called "Hopf bifurcation" for which, using the typical terminology of the linear stability analysis (LSA), an eigenvalue of the Jacobian matrix (in general a complex conjucate pair of eigenvalues) of the governing equations crosses the imaginary axis (i.e. the real part of the eigenvalue becomes positive with a corresponding value of imaginary part that is not zero [62]). For such a comparison, we have considered classical buoyancy convection in a cavity heated from below and cooled from above with conducting solid sidewall. As shown by Mizushima and Adachi [62] for Pr=7, this apparently innocuous system can take many and complicated routes to attain equilibrium or chaotic states, which involve (but are not limited to) textural transitions and 'multistability'. The latter concerns the ability of the flow to evolve along distinct branches of solutions, which exist in parallel in the space of parameters and stem from different initial conditions (coexisting 'attractors'). In particular, we have considered the specific dynamics occurring in the interval $47000<Ra<50000$ where, according to [62] (see Figs. 6 and 8 in their paper), the flow undergoes a subcritical Hopf bifurcations along a branch of evolution that originates from the point $Ra\cong49600$. Such a bifurcation is properly captured by the present solver as witnessed by the temperature and velocity

fields in Figs. 2 (showing the 'diagonal mode' of convection emerging as a result of the bifurcation) and the data (frequency of oscillation) in Table III.

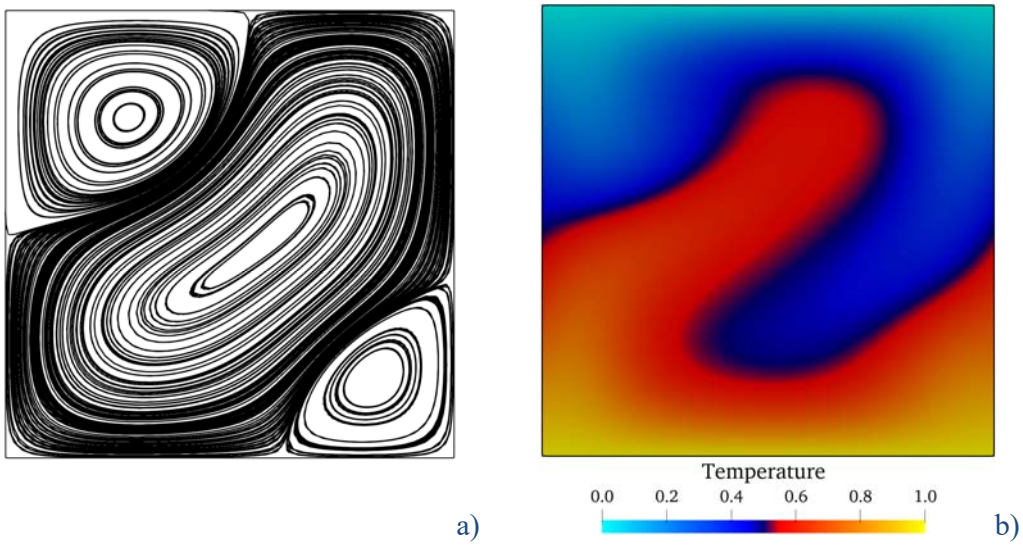

Figure 2: Snapshots of streamlines (a) and temperature distribution (b) for Rayleigh-Bénard convection in a square cavity with conducting sidewalls (Pr=7, *Ra*=48000, time-periodic state, see Table III for the related frequency).

Table III: Non-dimensional frequency f defined as $2\pi f^{Dim}\ L^2/\alpha$ where f^{Dim} is the dimensional frequency of the oscillation (Newtonian fluid, Pr=7, Rayleigh-Bénard convection in a square cavity with conducting sidewalls, uniform mesh: 10000 nodes, Hopf bifurcation, comparison with the results by Mizushima and Adachi [62]).

Data source	f
Mizushima and Adachi [62]	16.31
Present solver	16.19

Finally, some of the cases specifically considered in the present work (the FFS problem) have been also simulated (for different representative values of *Ra* and *Ri*) using different computational platforms, i.e. a commercial software (ANSYS Fluent) and the same code that [37] used to analyze the dynamics of thermal plumes in cross flow. Both rely on 2nd order upwind schemes (standard central differences being employed for the diffusive terms only). However, the software developed by [37] is completely explicit in time, whereas ANSYS Fluent is based on an implicit approach (moreover, in order to accelerate convergence, it takes advantage of a classical Algebraic Multigrid scheme (AMG) with standard parameters, i.e. the so-called Gauss-Seidel smoother [63]). Although OpenFoam (Sect. 2.4) and these alternate computational platforms rely on quite different numerical implementations, as witnessed by Table IV, the values obtained for the Nusselt number and the (non-dimensional) angular frequency of oscillation (ω) are in good agreement (the maximum percentage difference in the worst case being ≅5%).

Table IV: Properties of Hybrid Forced-buoyancy flow in the FFS configuration for various representative conditions. Comparisons of results obtained with different computational platforms (ω is the non-dimensional angular frequency; for unsteady regimes the time-averaged value of the Nusselt number is considered) .

Ri	*Ra*	Floor	Regime	Parameter	Parameter
∞	10^6	Adiabatic	Quasi-periodic	Present Nu_{step}^{horiz} : 9.86	Nu_{step}^{vert} 17.52
				Code by [37] Nu_{step}^{horiz} : 9.98	Nu_{step}^{vert} 17.94
∞	10^6	Hot	Periodic	Present Nu_{step}^{horiz} : 10.83	Nu_{step}^{vert} 3.01
				Code by [37] Nu_{step}^{horiz} : 10.80	Nu_{step}^{vert} 3.1
100	10^5	Adiabatic	steady	Present Nu_{step}^{horiz} : 3.23	Nu_{step}^{vert} 10.64
				ANSYS Fluent Nu_{step}^{horiz} : 3.19	Nu_{step}^{vert} 10.52
				Code by [37] Nu_{step}^{horiz} : 3.30	Nu_{step}^{vert} 10.66
1	10^7	Adiabatic	Unsteady with dominant frequency	Present Nu_{step}^{horiz} : 39.07	Nu_{step}^{vert} 45.41
				Code by [37] Nu_{step}^{horiz} : 40.12	Nu_{step}^{vert} 45.11
1	10^7	Hot	Unsteady with dominant frequency	Present Nu_{step}^{horiz} : 38.10	Nu_{step}^{vert} 16.58
				Code by [37] Nu_{step}^{horiz} : 39.50	Nu_{step}^{vert} 16.25
30	10^7	Adiabatic	Periodic	Present ω: 6280	
				Code by [37] ω: 6543	
1	10^7	Adiabatic	Unsteady with dominant frequency	Present ω: 3.58 10^4	
				Code by [37] ω: 3.77 10^4	
1	10^7	Hot	Unsteady with dominant frequency	Present ω: 3.38 10^4	
				Code by [37] ω: 3.2 10^4	

2.6 Mesh resolution and Kolmogorov length scale

The identification of a proper mesh, by which the dynamics that characterize the considered problems over different scales can be properly captured, requires a dedicated (separated) assessment. A relevant mesh must guarantee that the emerging solution does not depend on the used grid spacing. A parametric investigation must therefore be carried out considering different spatial resolutions until the percentage variation experienced by a representative physical quantity (e.g., the maximum fluid velocity or the flow frequency in the case of oscillatory solutions) falls below a given threshold (e.g., 2 or 3%). This is indeed the approach that has been used in the present work to identify the relevant uniform mesh for small or moderate values of the flow governing characteristic numbers, i.e. values of *Ra* up to O(10^6). Some results representative of the grid refinement study are summarized in Tables V and VI.

Table V: Non-dimensional frequency for different mesh sizes for the case of hybrid forced/buoyancy convection (Ri=100) with adiabatic bottom wall and Ra=4.7x10^5**.**

Mesh Size	f
1500x150	1.200 x10^3
1600x160	1.214 x10^3
1700x170	1.218 x10^3

Table VI: Non-dimensional frequency for different mesh sizes for the case of hybrid forced/buoyancy convection (Ri=30), with hot bottom wall and Ra=3x10^5**.**

Mesh Size	f
1600x160	6.983 x10^2
1700x170	6.912 x10^2
1800x180	6.924 x10^2

As an example, it can be seen that for the case with Ri=100, adiabatic bottom wall and Ra=4.7x10^5, for an increase of 200 points along the horizontal direction, the corresponding percentage variation in the frequency of oscillation lies below 2% (which explains why a mesh 1500x150 has been selected). The same concept applies to the case with Ri=30, hot bottom wall and Ra=3x10^5 for which the percentage variation is even smaller.

A more sophisticated strategy, however, has been implemented for larger values of Ra to ensure that the turbulent properties of the flow (eventually emerging in this range of the control parameter) are properly captured.

For such cases, we have estimated the needed resolution on the basis of the concept of Kolmogorov length scale (ζ). By definition this characteristic length indicates the *smallest flow feature* present in the considered flow (typically the size of the eddies where kinetic energy is dissipated due to viscous effects). It can also be seen as the length scale that bounds from below the process of energy transfer from large scales to smaller scales (which is typical of turbulent flow, [64-66]).

As it represents the scale where the energy injected into the system due to an external driving effect (it being inertia due to an imposed injection fluid velocity or buoyancy for forced and natural convection, respectively) is finally dissipated (converted in internal energy due to friction), the length ζ obviously depends on the characteristic numbers that measure the relative importance of such effects (namely the Reynolds and/or the Rayleigh number). Available correlations in the literature indeed confirm this way of thinking.

According to (Pope [67]), as an example, for forced flow, the Kolmogorov length scale can conveniently be evaluated as:

$$\zeta_{\mathrm{Re}} \cong \mathrm{Re}^{-3/4} \tag{18}$$

Similarly, for thermal convection, ζ can be put in direct connection with the Rayleigh number. In this case, however, available correlations differ depending on the dominant mechanism driving buoyancy (which is of the Hadley or RB type depending on whether the prevailing temperature gradient is perpendicular or concurrent to gravity, respectively).
In the first case, as indicated by Paolucci [68] and Farhangnia et al. [69]:

$$\zeta_{Ra\perp} = \pi\left(\frac{16\,\mathrm{Pr}}{Ra}\right)^{3/8} \tag{19}$$

In the second situation, according to Kerr [70] and De et al. [71]:

$$\zeta_{Ra\parallel} = 1.3Ra^{-0.32} \tag{20}$$

A conservative approach for the situation in which many concurrent mechanisms of convection are effective is generally based on the selection of the smallest possible value of ζ (see, e.g., Lappa and Gradinscak [72], Lappa and Inam [38]), i.e.

$$\zeta = \min\left\{\zeta_{\mathrm{Re}}, \zeta_{Ra\perp}, \zeta_{Ra\parallel}\right\} \tag{21}$$

In agreement with the earlier study by Lappa and Inam [38], for all the situations considered in the present work with Ra>O(10^5) we have found $\zeta_{Ra\parallel}$ to be the most restrictive condition controlling the size of the mesh regardless of the considered value of Ri. For turbulent states, mesh convergence has been judged on the basis of the frequency spectrum (by verifying that the (-5/3) scaling trend predicted by the Kolmogorov law is independent from the mesh in terms of velocity amplitude and related frequency distribution, see Sect. 4 for the related plots). Using the set of criteria described in the present section, the required numerical resolution has been determined for each considered case (the needed number of point ranging from a minimum of 400x40 to a maximum of 2000x200 depending on the considered value of the Rayleigh number).

3. Results

The layout of this section is as follows. Each sub-section represents a self-contained discussion of the patterning behavior for a fixed value of the Richardson number. In particular, Sect. 3.1 is concerned with the results for pure buoyancy convection (formally corresponding to $Ri\rightarrow\infty$); Sect. 3.2 describes the outcomes of the simulations for circumstances where, though forced convection is present (finite values of Ri), buoyancy still plays a dominant role (Ri=100 and Ri=30); Sect. 3.3 examines small-Ri behavior (representing the idealized situation in which forced flow and buoyancy convection have a comparable magnitude). The value of the Prandtl number has been fixed to Pr=1.

A critical comparison of the different situations, leading to general conclusions on the overall bifurcation and heat transfer scenarios, is finally elaborated in Section 4.

3.1 Pure buoyancy case

As outlined above, the first section contains material that provides a foundation for the rest. Being entirely focused on pure buoyancy convection, it immediately supplies the reader with a clear account of the considered interval of values of the Rayleigh number and the typical convective modes that this type of flow can produce in such a range of *Ra* (for the two variants of thermal boundary conditions at the bottom wall defined by eq. (9)). Related results are summarized in Figs. 3-6. As further elaborated in Sect. 4, these dynamics can be used as a basis to disentangle the role played by buoyancy effects in more complex situations where the Richardson number takes finite values.

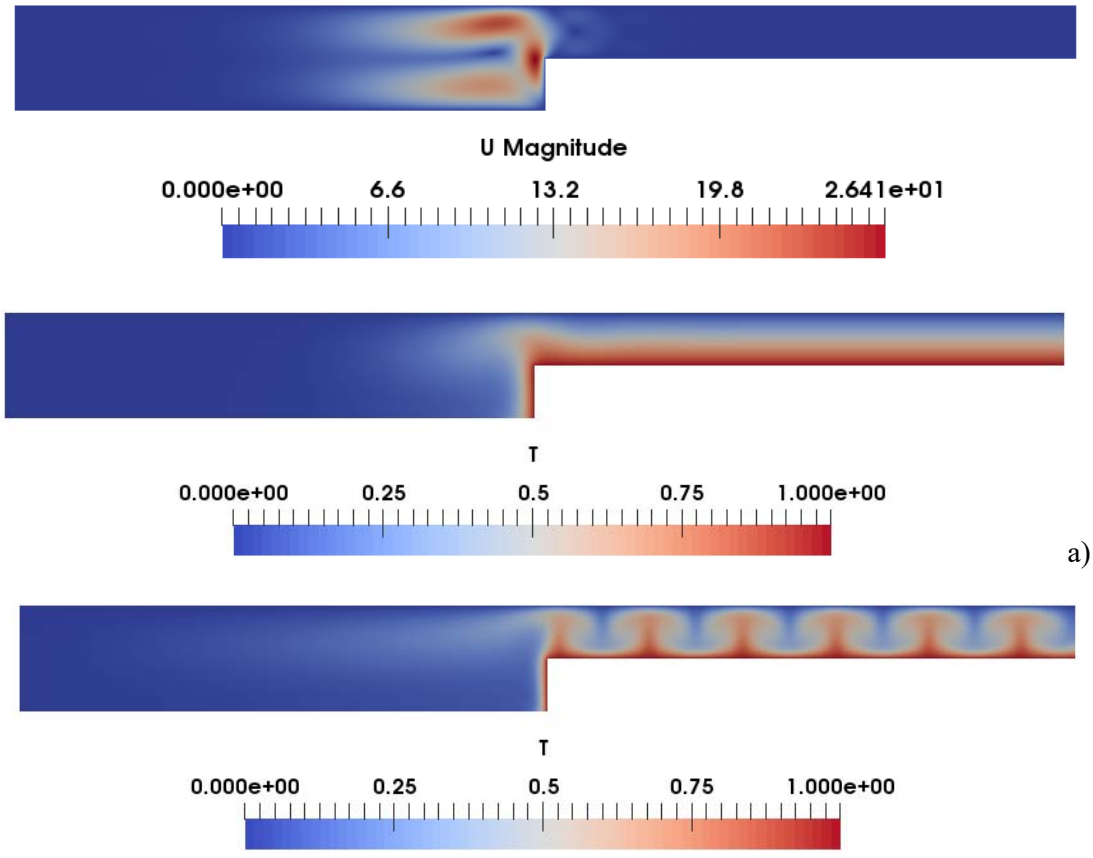

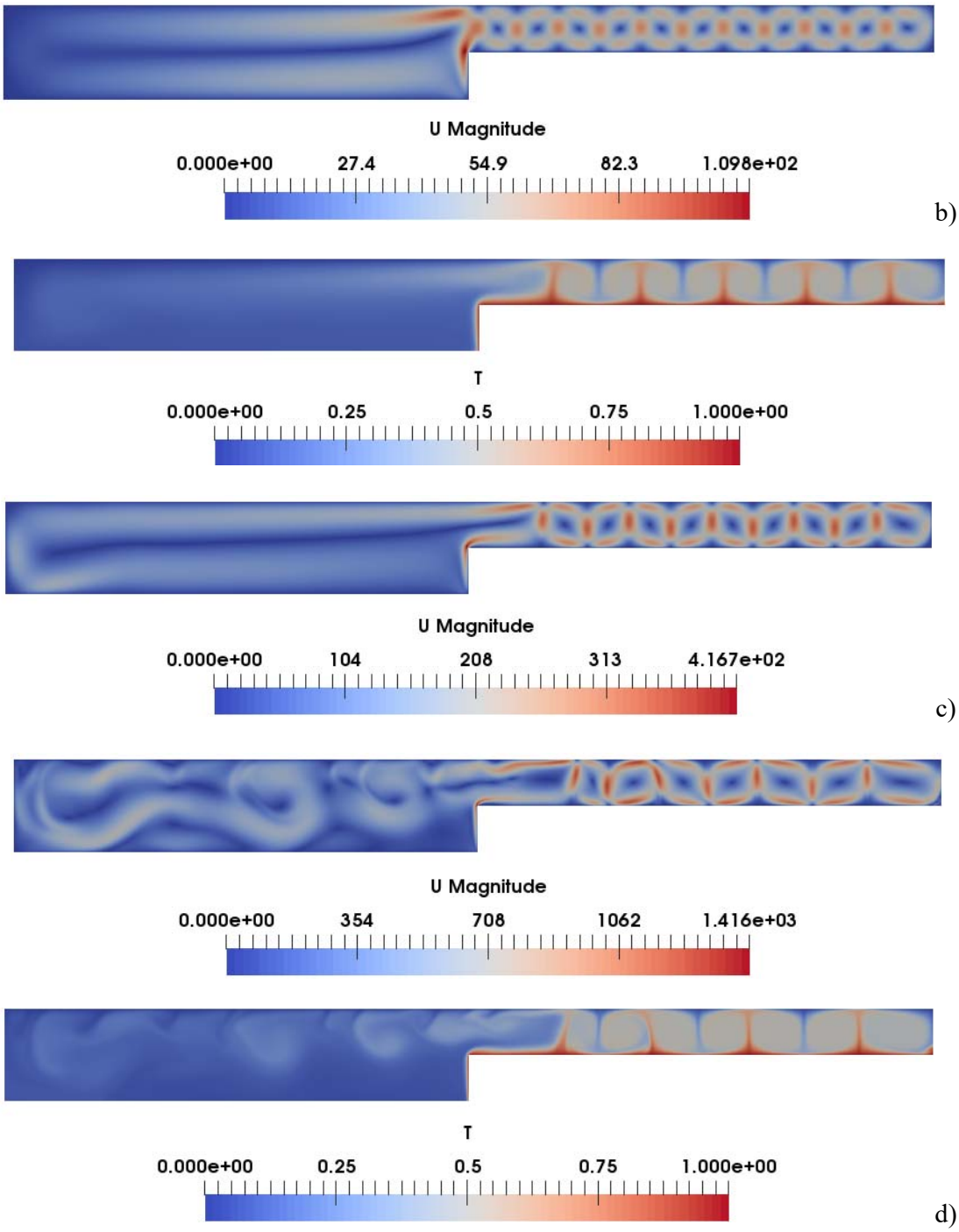

Figure 3: Snapshots of velocity field and temperature distribution for the case of pure buoyancy convection and cavity with adiabatic bottom wall: a) $Ra=10^4$, b) $Ra=10^5$, c) $Ra=10^6$, d) $Ra=10^7$.

Following a logical approach we start from the simplest possible case that is the situation with $Ra=10^4$ and bottom wall ($0<x<A/2$) with adiabatic conditions. As evident in the velocity distribution (see the top view reported in Fig. 3a), a strong circulation is created in the left part of the domain (the region characterized by larger cross-sectional area). As also revealed by the inclined thermal plume originating from the corner of the step, this circulation of the *Hadley type* is

essentially driven by the vertical heated sidewall of the step. Less evident in this figure is the presence of small rolls formed in the shallow region constrained between the top rigid boundary and the top surface of the step. Unlike the other larger vortex (occupying the region x<A/2), these (nine) rolls may be regarded as the manifestation of the almost pure *Rayleigh-Bénard convection*, which emerges as a result of the prevailing vertical temperature gradient established for x>A/2. These rolls are weak as witnessed by the presence of an almost undisturbed thermal boundary layer, which is relatively thicker in comparison to the one formed on the vertical wall. The Hadley flow being developed in the left part of the domain (x<A/2) is dominant in terms of strength. Despite the inherent complexity of the overall convective configuration (which features two coexisting modes of convection), the two convective mechanisms exist in an almost independent way and the overall flow is steady.

For Ra=1x10^5 (Fig. 3b), the Hadley flow and RB convection have comparable strength. An interesting change can also spotted in the number of small rolls located above the step, which increases from nine to eleven. A big transverse roll (Hadley flow) is still steadily located in the entire left portion of the cavity. The maximum velocity magnitude is attained just before the section where there discontinuity in the cross-sectional area occurs, i.e. along the vertical heated wall of the step (x≅A/2). In terms of temperature distribution, well-defined thermal plumes are formed for x>A/2 whereas for x<A/2 the fluid is relatively cold and undisturbed. As time passes the plume lobes remain distinct and are not significant deformed. A hot thin boundary layer is formed on the vertical wall of the step. The flow is still steady.

If the Rayleigh number is further increased (Ra=1x10^6 in Fig. 3c), interestingly, there is a decrease in the number of flow features visible in the right portion of the cavity. The number of velocity rolls formed in this case comes back to nine (same as for Ra=1x10^4). As revealed by Fig. 3c, this effect is the result of the *coalescence* of the first roll of RB nature with the larger circulation of the Hadley type developing in the left part of the domain. Notably, in such conditions each plume has a thin, sharp stem with a well-defined cap and lobes that are significantly deformed by vortex structures, which means that the plumes established in the cavity for Ra=1x10^6 pertain to the so-called IVND regime (the so-called Inviscid-Nondiffusive Regime according to the classification originally elaborated by Hier Majumder et al. [73]). This regime takes place for high Rayleigh number (Ra > O(10^6) and Prandtl number near 1. Most remarkably, for such conditions the flow is unsteady (quasi-periodic) as shown in Fig. 4.

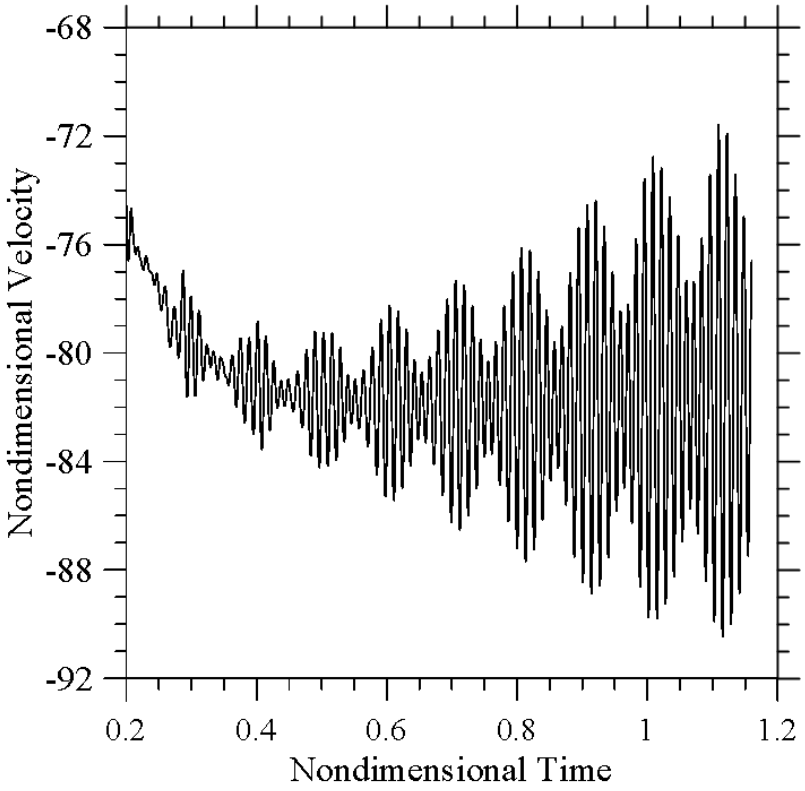

Figure 4: Velocity (horizontal component) signal for Ra=10^6 and adiabatic bottom measured by a numerical probe located at (0.25, 0.75).

Finally, for Ra=1x10^7 (Fig. 3d), a further decrease in the number of RB rolls occurs due to enhancement of the aforementioned coalescence process (by which the RB rolls are absorbed by the elongated circulation occupying the left region). The most evident change, however, concerns the region with large cross-sectional area. The initially unicellular (Hadley) roll established there is broken into distinct vortices, which travel continuously from left to the right (their average number in time being three). This phenomenon is produced by a *wave travelling towards the left* along the top boundary of the duct (clearly visible in the temperature distribution). More precisely, it manifests itself through the periodic shooting of 'packets' of hot fluid in the cold fluid located in the left region of the cavity. Such disturbances originate from the head of the plume formed close to the corner of the step (x≅A/2) and travel towards the left, i.e. in the downstream direction (in other words, the wave uses the leftward-directed branch of the Hadley cell as a substrate for propagation (we will come back to this phenomenon, which is typical of the Hadley flow for Pr≅1 in cavities subjected to horizontal temperature gradients, later).

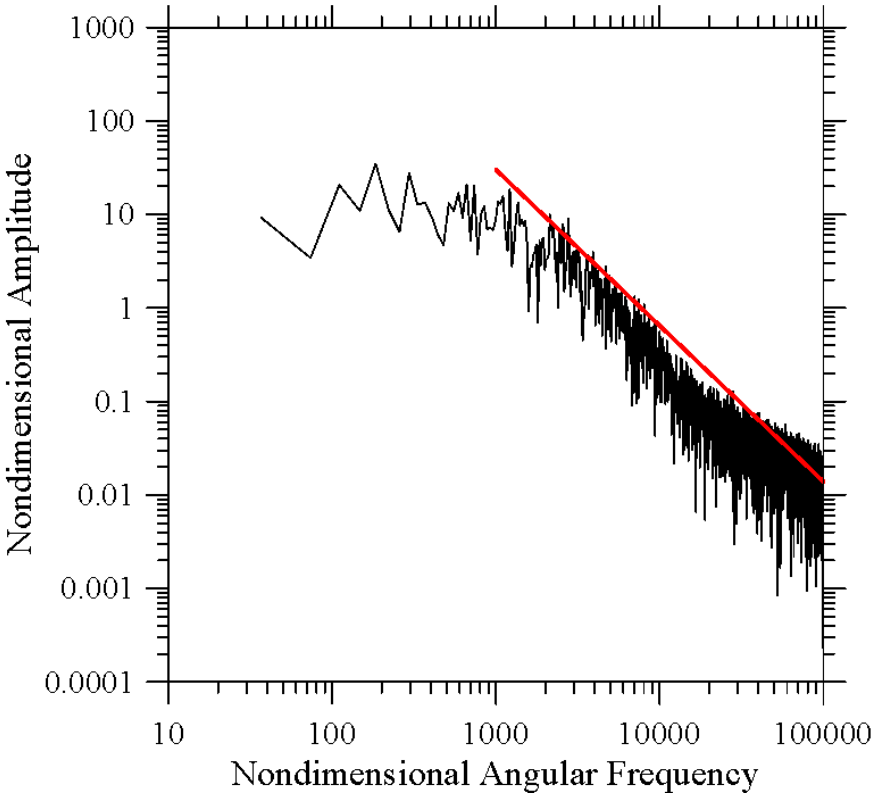

Figure 5: Frequency spectrum for $Ra=10^7$ and adiabatic bottom. The red straight line indicates the (-5/3) scaling trend predicted by the Kolmogorov law.

In such conditions the flow is moderately turbulent as witnessed by the frequency spectrum shown in Fig. 5 (see also Table VII). In agreement with the expected behavior of turbulence on small length scales (the so-called self-similarity property of turbulence, [63-66]), the spectrum *aligns with a* $\omega^{-5/3}$ *law* in a certain range of (high) frequencies.

After discussing the different situations for the cavity with a hot step and adiabatic bottom wall, it is also worth examining the other configuration (differing in regard to the thermal boundary condition used for the bottom wall, kept at constant temperature, see Fig. 6).

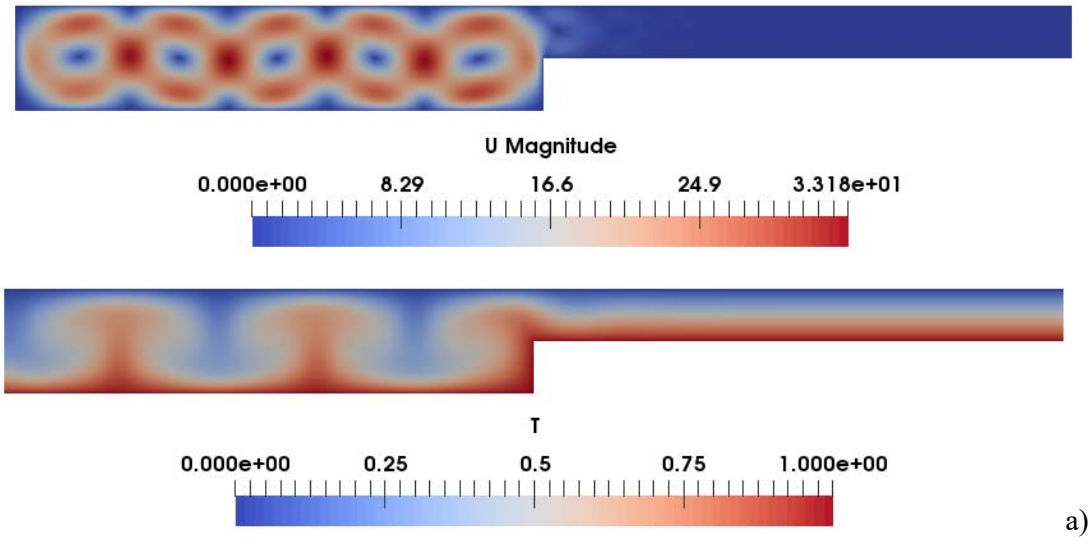
U Magnitude
0.000e+00
8.29
16.6
24.9
3.318e+01
T
0.000e+00
0.25
0.5
0.75
1.000e+00

a)

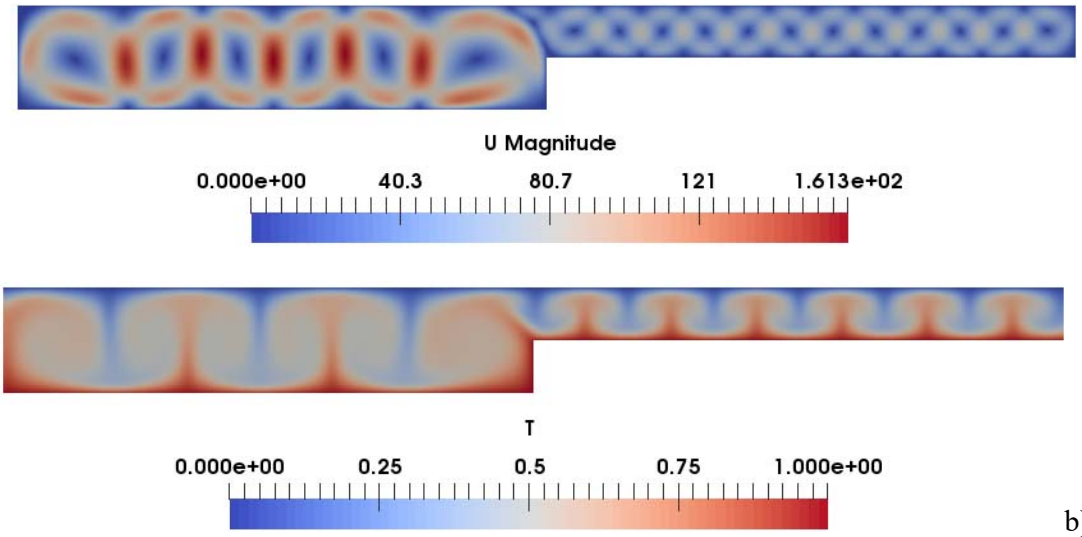
U Magnitude
0.000e+00
40.3
80.7
121
1.613e+02
T
0.000e+00
0.25
0.5
0.75
1.000e+00

b)

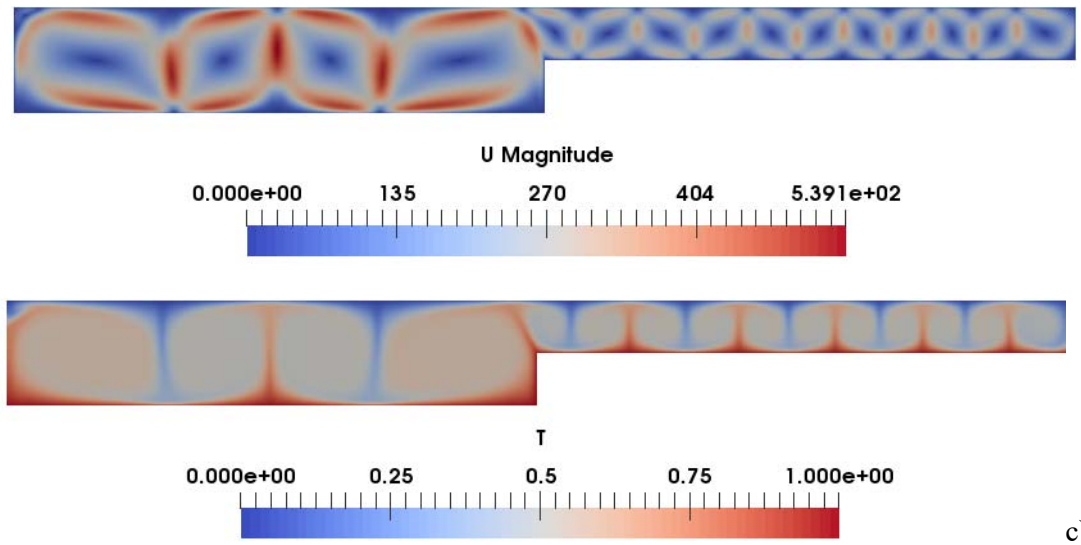
U Magnitude
0.000e+00
135
270
404
5.391e+02
T
0.000e+00
0.25
0.5
0.75
1.000e+00

c)

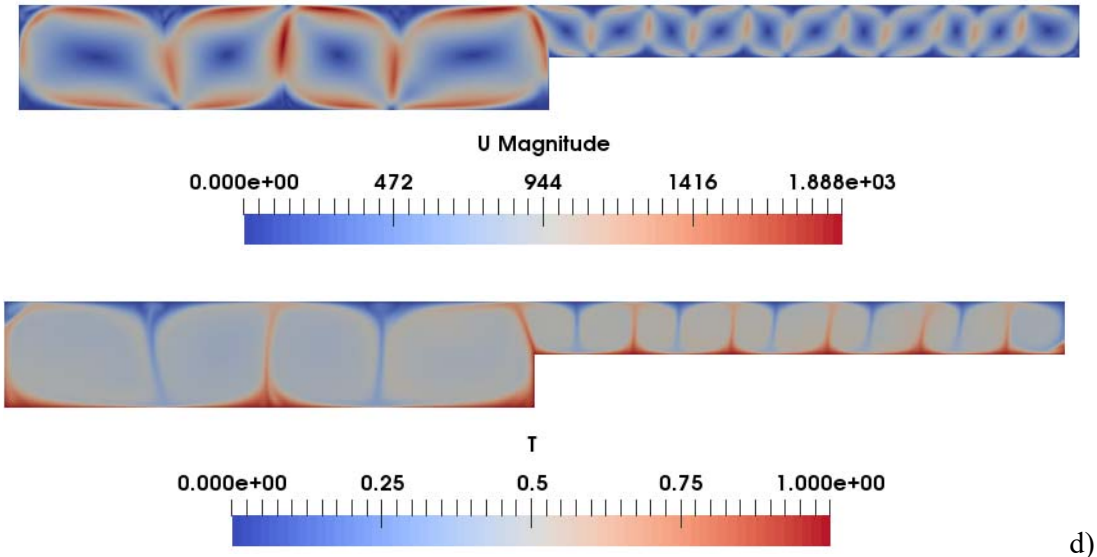

d)

Figure 6: Snapshots of velocity field (left) and temperature distribution (right) for the case of pure buoyancy convection and cavity with hot bottom wall: a) Ra=10^4, b) Ra=10^5, c) Ra=10^6, d) Ra=10^7.

As qualitatively illustrated by Fig. 6a, for Ra=1x10^4 again nine weak small velocity rolls can be seen in the shallow region above the step (as for the adiabatic-floor case). However, five medium-sized velocity rolls are now present in the left half portion of the cavity. They are clearly rolls of RB nature as indirectly demonstrated by the simultaneous development of evenly spaced thermal plumes. The different distortions undergone by the temperature field in the left and right regions of the cavity qualitatively substantiate the realization that convection produced for x<A/2 is much stronger than that of the same nature emerging for x>A/2. This trend can be immediately explained simply taking into account the cubic dependence of this form of convection on the vertical extension of the considered layer of fluid (d/2 for x>A/2 corresponding to an effective value of the Rayleigh number Ra_{eff}=Ra/8). The flow is steady in both sides of the cavity.

On increasing Ra to 10^5, thermal plumes become a pervasive feature of the temperature pattern (Fig. 6b). All plumes have a vertical stem with the exception of that originating from the step corner, which is inclined to the left. The number of small (right region) and large (left region) rolls increases from nine to twelve and from five to six, respectively, which indicates that (as expected) the Rayleigh number has a significant influence of the emerging wavenumber. The most remarkable change, however, concerns the spatio-temporal behavior of the flow, which becomes *unsteady*.

This finding indicates that transition to time-dependent flow can be obtained with a smaller value of the Rayleigh number when the configuration with the heated bottom is considered (Ra had to be increased to Ra=10^6 to observe similar phenomena for the adiabatic wall case; we will come back to these aspects in Sect. 4 where detailed information about the hierarchy of bifurcations will be provided).

For Ra=1x10^6 (Fig. 6c), there is a decrease in the number of rolls (from twelve to eleven) in the right portion of the cavity (the same process was observed for the adiabatic floor case). A similar trend is effective for the rolls located in the left region (their number being reduced from six to four). The shrinkage in the number of rolls essentially results from roll coalescence phenomena.
When the Rayleigh number is finally increased to Ra=1x10^7 (Fig. 6d), no change occurs in terms of patterning behavior. However, the flow becomes weakly turbulent (see Table VIII) and we ascribe the less chaotic nature of the flow (with respect to the equivalent case with the adiabatic floor) to the lack of a wave-propagation mechanism such as that visible in Fig. 3d (requiring the presence of horizontal currents of the Hadley type).

3.2 Mixed convection for Ri=100 and Ri=30

We turn now to considering the case where the buoyancy flow, naturally produced by the heated surfaces embedded in the physical domain, *interacts with cold fluid being injected from the left*, which leads to a typical problem of mixed forced-buoyancy convection (Figs. 7-9).
On the basis of the same approach undertaken in Sect. 3.1, snapshots of the thermo-fluid-dynamic fields for increasing values of the Rayleigh number and Ri=100 are orderly collected in Figs. 7 and 8 for the two aforementioned archetypal situations with adiabatic and hot bottom wall, respectively.
The simplest situation is that presented in Fig. 7a for Ra=1x10^4. It is shown that the cold fluid entering through the inlet continues to travel straight with a moderate velocity until it comes in contact with the hot obstruction (the step). The hot step causes the velocity to increase due to the contraction of the cross-sectional area and the incompressibility constraint. Moreover, a thick hot boundary layer develops along the entire length of the horizontal and vertical walls of the step. The increasing thickness of the thermal boundary layer in the downstream direction is obviously a consequence of the heat being released by the hot surface of the step in the region x<A/2.
The next figure of the sequence (Fig. 7b) simply illustrates that if the Rayleigh number is increased by one order of magnitude (Ra=1x10^5 and Re grows accordingly due to the Ri=const=100 condition, i.e. Re≅31.6), the thickness of the boundary layer becomes smaller. This can obviously be ascribed to the larger amount of cold fluid being injected in the system per unit time as a consequence of the increase in the Reynolds number. The flow remains steady as it was for Ra=10^4.

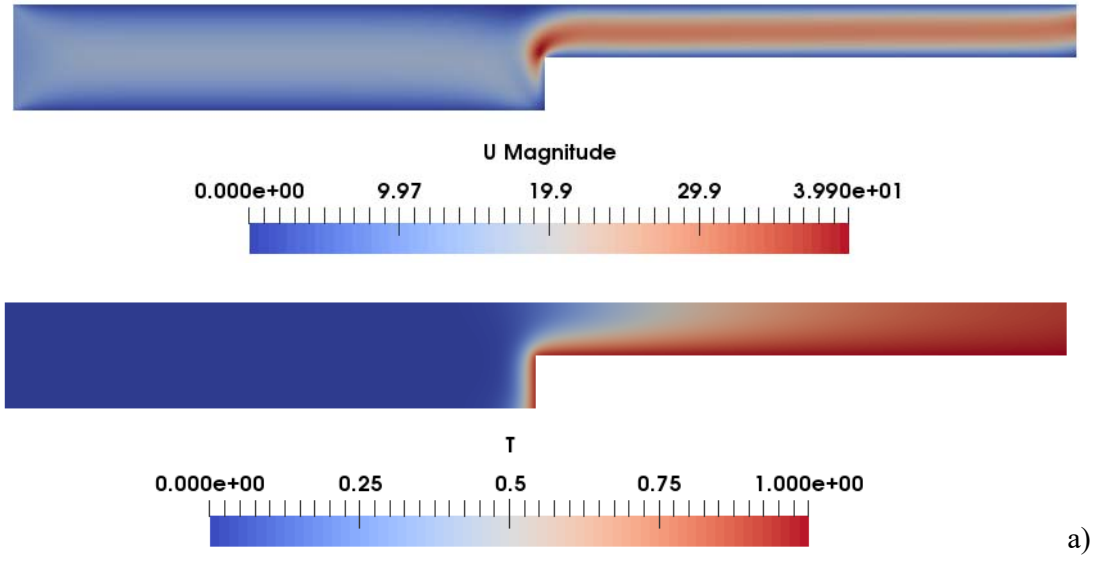
U Magnitude
0.000e+00
9.97
19.9
29.9
3.990e+01
T
0.000e+00
0.25
0.5
0.75
1.000e+00

a)

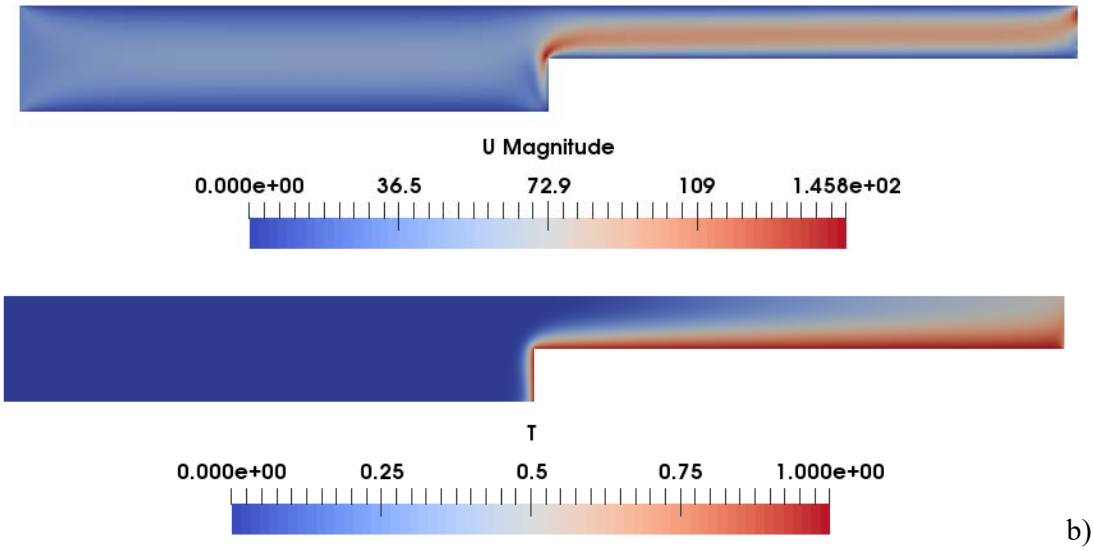
U Magnitude
0.000e+00
36.5
72.9
109
1.458e+02
T
0.000e+00
0.25
0.5
0.75
1.000e+00

b)

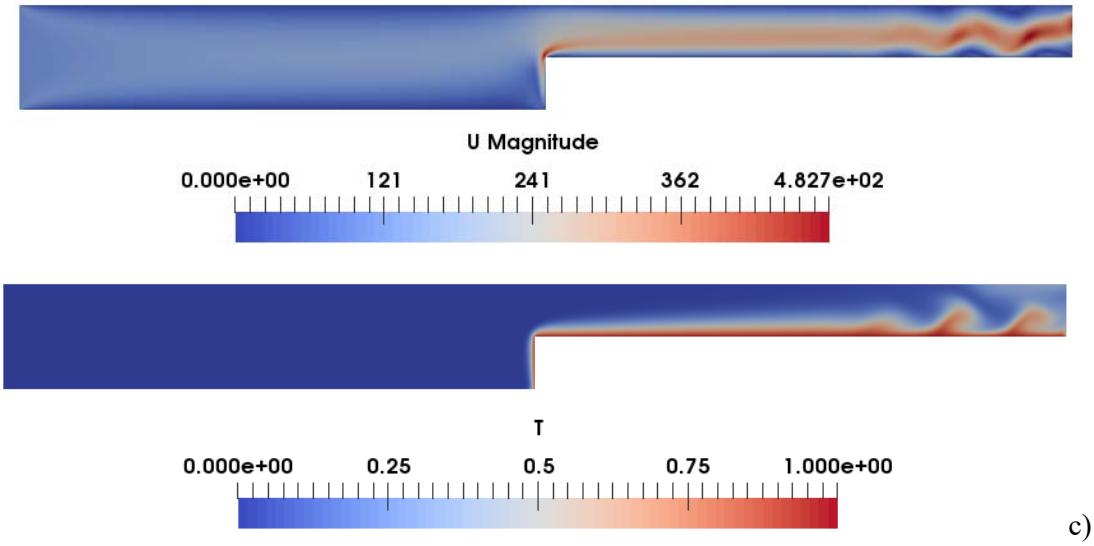
U Magnitude
0.000e+00
121
241
362
4.827e+02
T
0.000e+00
0.25
0.5
0.75
1.000e+00

c)

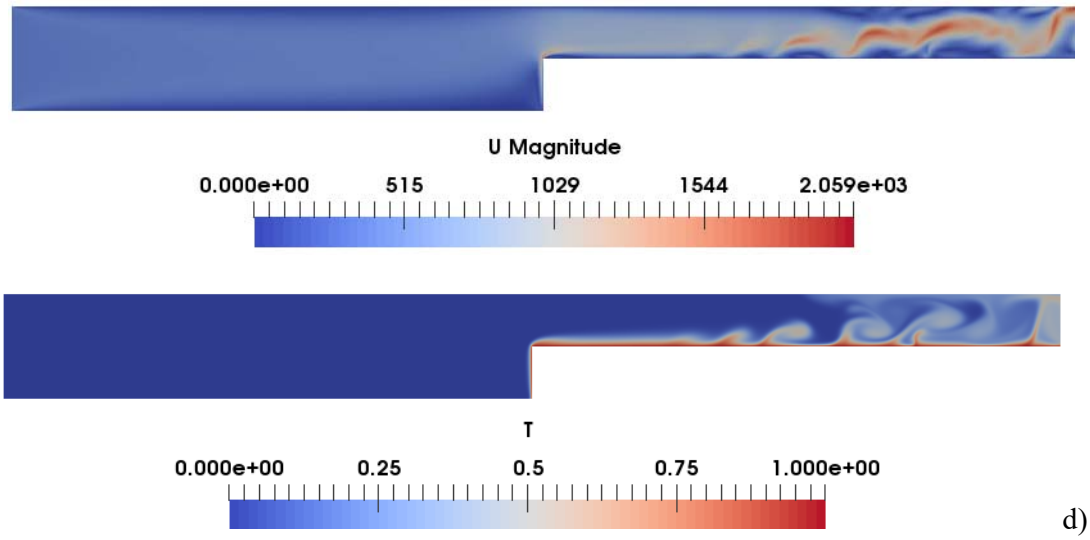

d)

Figure 7: Snapshots of velocity field (left) and temperature distribution (right) for the case of hybrid forced/buoyancy convection (Ri=100), coaxial inflow and outflow sections and cavity with adiabatic bottom wall: a) Ra=10^4, b) Ra=10^5, c) Ra=10^6, d) Ra=10^7.

A notable change, however, starts to affect the dynamics for Ra=1x10^6 (Fig. 7c). A Hopf bifurcation takes place and the flow evolves accordingly from a steady regime to a time dependent one. Some sinusoidal distortions can be seen in the topological development of the main current located above the step. These disturbances seem to be directly correlated to the thermal features that can be seen in the temperature distribution. Where the concavity of the stream centerline is towards the bottom (velocity field), a thermal plume is visible in the temperature field and, vice versa (concavity towards the top corresponds to plume absence). These convective and thermal localized phenomena appear at a certain distance from the leading edge, i.e. the corner of step (approximately a non-dimensional distance 5 times the height of the fluid located above the step, i.e. $l \cong 5/2$). The number N of visible convective distortions is on average equal to 3. These plumes do not hold a fixed position, rather they continuously travel in the downstream direction. However, it is important to remark that the fluid has not yet entered the turbulent phase (the flow being still in a quasi-periodic condition, not shown).

A further increase in the order of magnitude of the Rayleigh number (Ra=1x10^7, Re≅316, Fig. 7d) causes (as expected) transition to a more chaotic state. The thermal boundary layer becomes very thin. The distortions affecting the main stream above the step are no longer regular and evenly distributed in space (this being reflected by an equivalent behavior of the thermal plumes). The increase in Ra at fixed Ri has also another notable consequence. Plumes are produced *at a much smaller distance from the leading edge* ($l \cong 2$). Moreover, their *extension in the vertical direction is generally smaller* than that seen for Ra=1x10^6, which can be interpreted taking into account the dual influence of a simultaneous increase of Ra and Re. In such a context, indeed, it is worth recalling that in standard RB convection, plume caps are known to become progressively smaller as

the Rayleigh number becomes higher (see, e.g., Lappa [74]). Superimposed on this is the effect of the Reynolds number. As this parameter (the inflow velocity) grows, plumes have less time to develop in the vertical direction before they are transported towards the outflow section and leave the domain through it (the reader being also referred to Lappa [37] for some equivalent considerations elaborated in the case of thermal plumes interacting with a free cross flow).

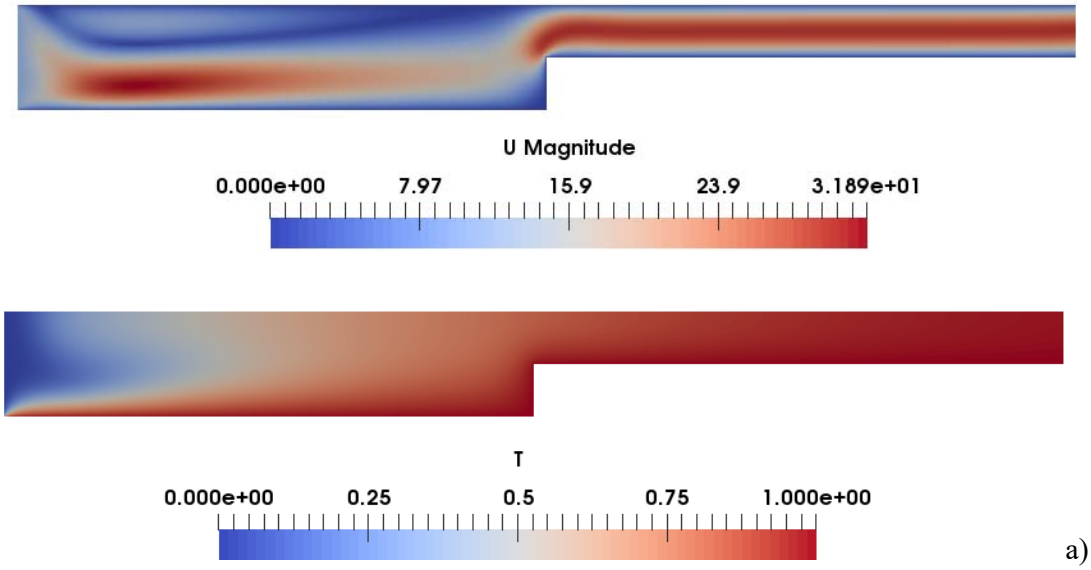

a)

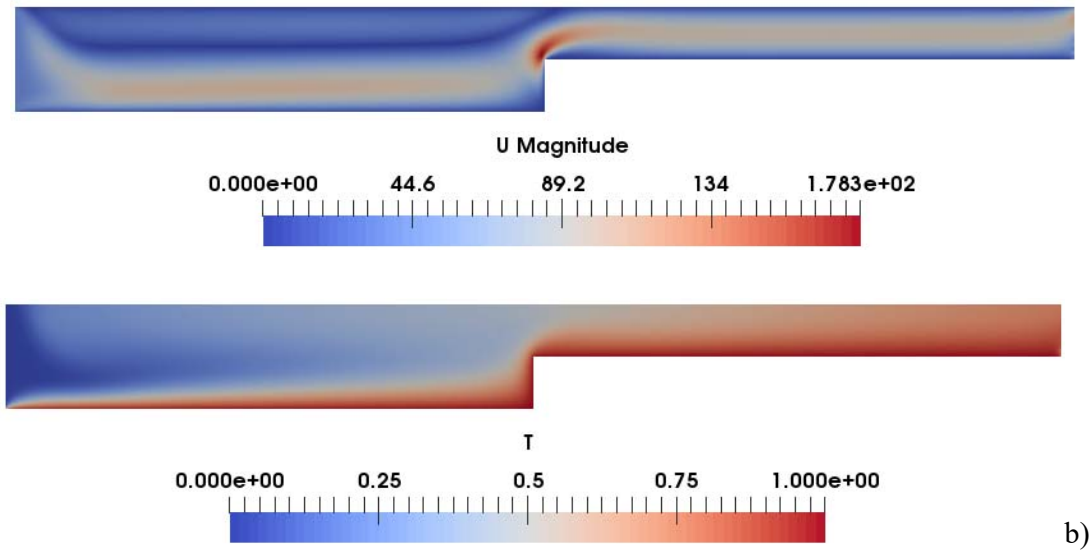

b)

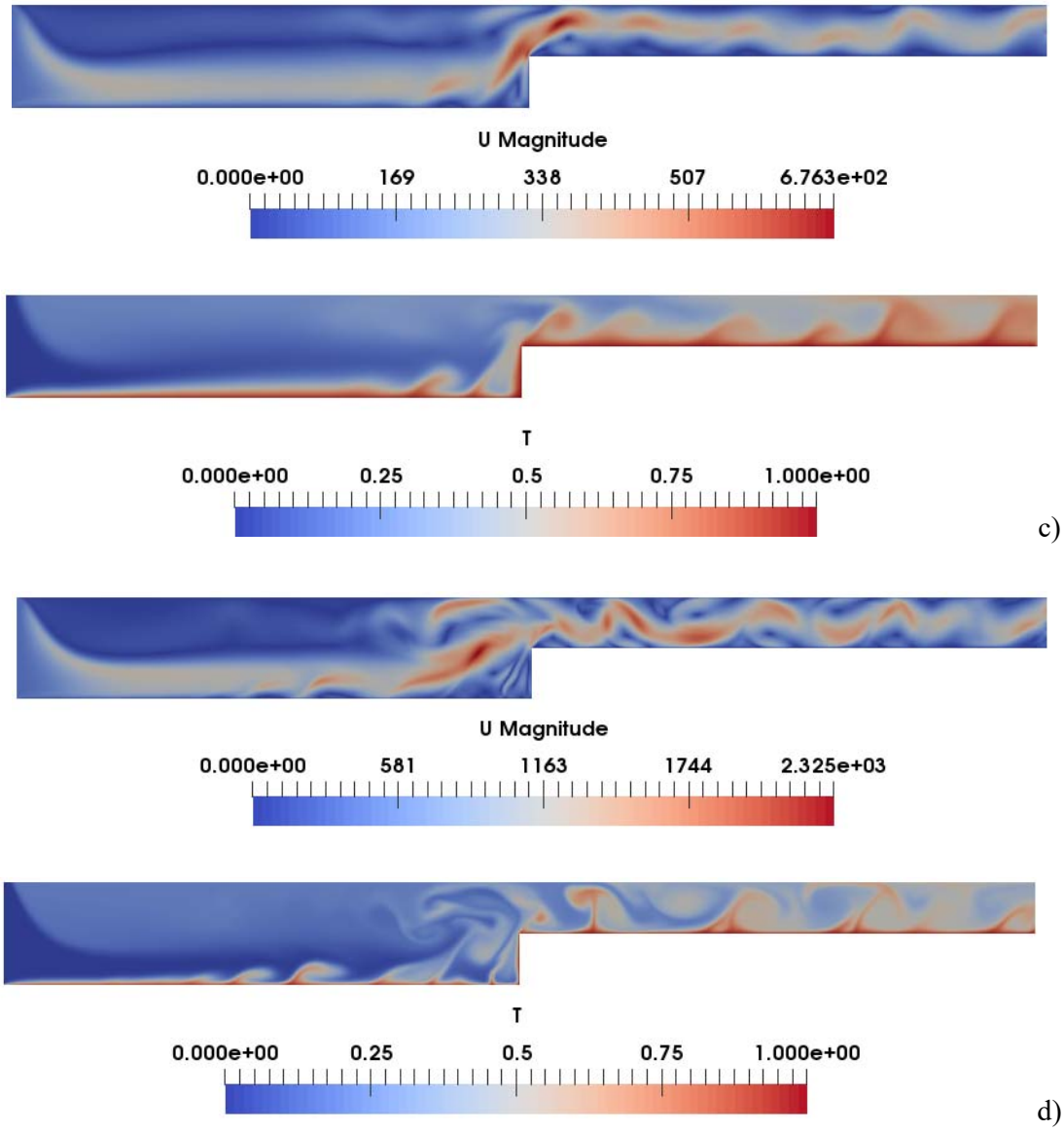

Figure 8: Snapshots of velocity field (left) and temperature distribution (right) for the case of hybrid forced/buoyancy convection (Ri=100), coaxial inflow and outflow sections and cavity with hot bottom wall: a) Ra=10^4, b) Ra=10^5, c) Ra=10^6, d) Ra=10^7.

Figure 8 shows the equivalent dynamics when the condition of adiabatic floor is replaced with that of wall at constant temperature.

In line with what one would expect on the basis of simple physical arguments (see Fig. 8a), "heat island" effects can be produced in the region located above the step (as a result of the increased amount of heat being transferred for x<A/2 from the solid boundary to the fluid). A significant change also becomes effective in the left portion of the cavity. A roll, adjacent the top wall and stretched in the horizontal direction, is created just after the inflow section. Owing to this convective effect, the fluid entering the system from the left is deflected towards the bottom and its velocity greatly increases (the maximum velocity being comparable to that obtained in the region of

fluid located above the step). The cold fluid takes a downward route and travels very close to the floor for a while (x<A/2). As soon it reaches the hot step (x≅A/2) it is forced to rise, spreads itself in the right half portion of the domain and then continues to travel undisturbed in the downstream direction. For Ra=1x10^5 (Fig. 8(b)), no significant differences can be highlighted with regard to the flow topology and structure. In terms of temperature distribution, however, a mitigation of the above-mentioned heat island effect can be noticed (due to the increased amount of cold fluid being injected in the cavity per unit time).

The complexity of the velocity field starts to grow as soon as the Rayleigh is set to the value Ra=1x10^6 (Fig. 8c). The flow becomes time-dependent. As it is evident from the temperature distribution, thermal plumes now originate directly from the surface of the hot floor (x<A/2) and travel to the right. When a plume of such a series meets the hot vertical surface of the step, *it merges with the related (vertical) thermal boundary layer producing a disturbance* (a bulge in the thickness of the boundary layer) *directed upwards*. This disturbance is then transferred to the horizontal branch of boundary layer (developing from the leading edge of the step in the same direction of the prevailing flow, i.e. from left to right). Accordingly, a train of traveling plumes can be recognized above the entire horizontal surface of the step, which formally behaves as a wave propagating in the downstream direction.

The final increase in the Rayleigh number to Ra=1x10^7 (Fig. 8(d)), makes the velocity field more involved. Again plumes originating from the extended surface of floor (x<A/2) and step (x>A/2) can be seen. The plumes have thin, sharp stem with well defined cap and lobes that are considerably deformed by vortex structures. As the reader will immediately realize by inspecting Fig. 9b, the velocity frequency spectrum is moderately turbulent and relatively similar to that obtained for the configuration with adiabatic bottom (Fig. 9a). Both align with the Kolmogorov law for ω in the range between 4x10^3 and 10^5.

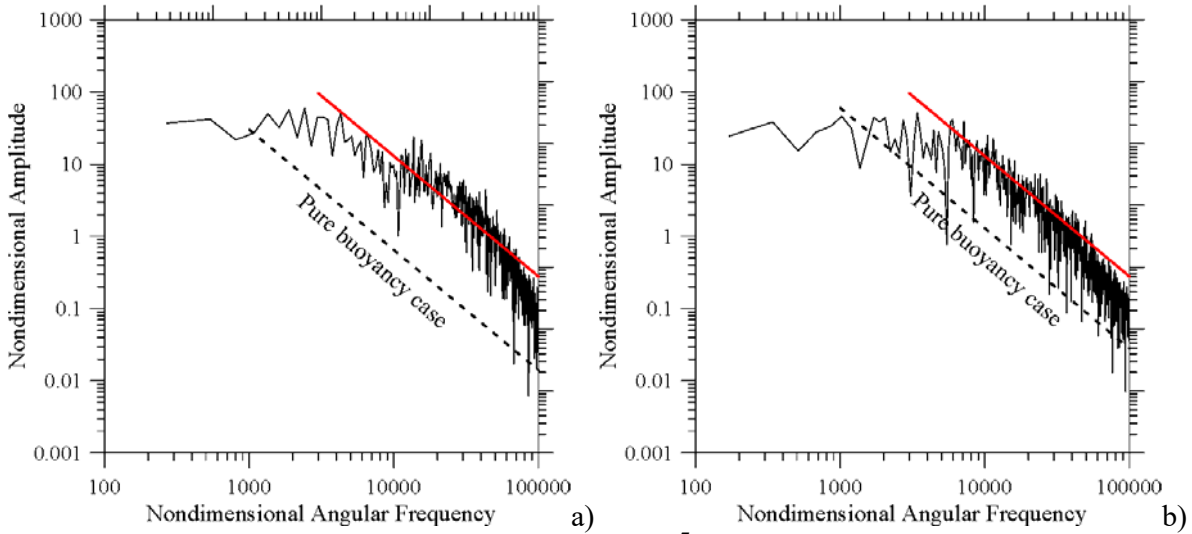

Figure 9: Frequency spectrum for Ri=100 and Ra=10^7: a) adiabatic bottom, b) Hot bottom. The dashed line indicates the corresponding trend for the pure buoyancy case ($Ri\rightarrow\infty$).

Comparison with the corresponding trend obtained in the pure buoyancy case (see the dashed line), indicates that the overall spectrum is shifted to the right, i.e. that for *Ri*=100 the energy tends to reside on smaller temporal scales (which indirectly confirms that new instability mechanisms are enabled with respect to the situation with pure buoyancy convection considered in Sect. 3.1).
We do not show the snapshots of temperature and velocity fields for *Ri*=30 as they are qualitatively similar to those for *Ri*=100. However, precise information about the dependence of heat transfer on the problem parameters (as quantitatively substantiated through the Nusselt number vs *Ra* and *Ri*) is reported in the form of dedicated tables (the Reader being referred to Tables VII and VIII).

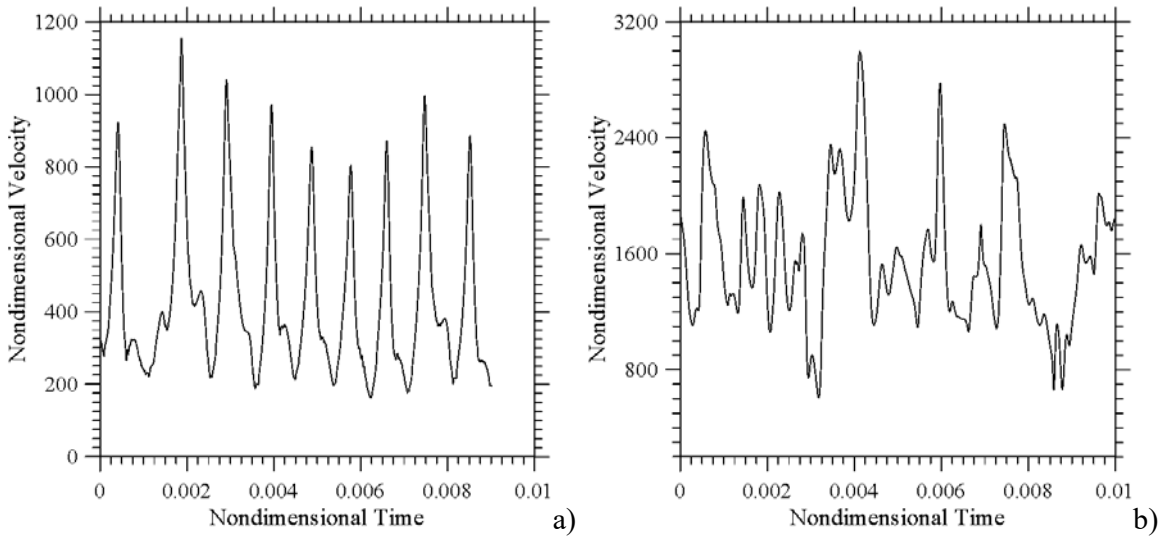

Figure 10: Velocity (horizontal component) signals for *Ri* =30 and $Ra=10^7$ provided by probes located in the region with reduced cross-sectional area (x>A/2): a) adiabatic floor case (probe point (9.5, 0.6)), b) hot floor case (probe point (5.5, 0.7)).

For this specific value of the Richardson number (*Ri*=30), we limit ourselves to considering the behavior of the velocity signals for $Ra=10^7$. Insights into the role played by the thermal boundary conditions for this condition can immediately be gathered from Fig. 10. Indeed, as a fleeting glimpse into the right and left panels of this figure would immediately reveal, the signal for the adiabatic case displays a much more contained amplitude and a simpler frequency spectrum; this apparently innocuous observation should be regarded as an important clue for a notable difference in the related hierarchy of bifurcations (as we will clarify further in Sect. 4.1).
Figures 10a and 10b are instructive also for another reason. They clearly illustrate that every time a thermal plume passes through a given observation point (the probe location indicated in the figure caption) a peak is produced in the corresponding horizontal component of the velocity. Such an increase can obviously be ascribed to the additional 'blocking' effect produced by the vertical eruptions of hot fluid (formally behaving as an additional obstruction in the flow forcing it to increase locally its horizontal velocity in order to conserve the volumetric flow rate).

3.3 Mixed convection for Ri=1

This section is devoted to the situation where forced and buoyancy convection have *comparable strength*, i.e. Ri=1. Since the numerical results for Ra=10^4 and 10^5 simply show regular and laminar (steady) flow, for the sake of conciseness, we do not describe them in detail (the reader being referred again to Tables VII and VIII for some related quantitative details).

Interestingly, as revealed by Fig. 11a, though for Ra=10^6 and adiabatic floor no thermal plumes can be identified, some "corrugation" pops up in the shape of both the kinematic and thermal boundary layers developing along the top wall of the step (x>A/2). A further increase in the Rayleigh number to Ra=1x10^7 (Fig. 11b) results in a slightly more complex velocity field. A horizontally stretched recirculation zone can be clearly observed on the surface of top wall of the step just after the corner.

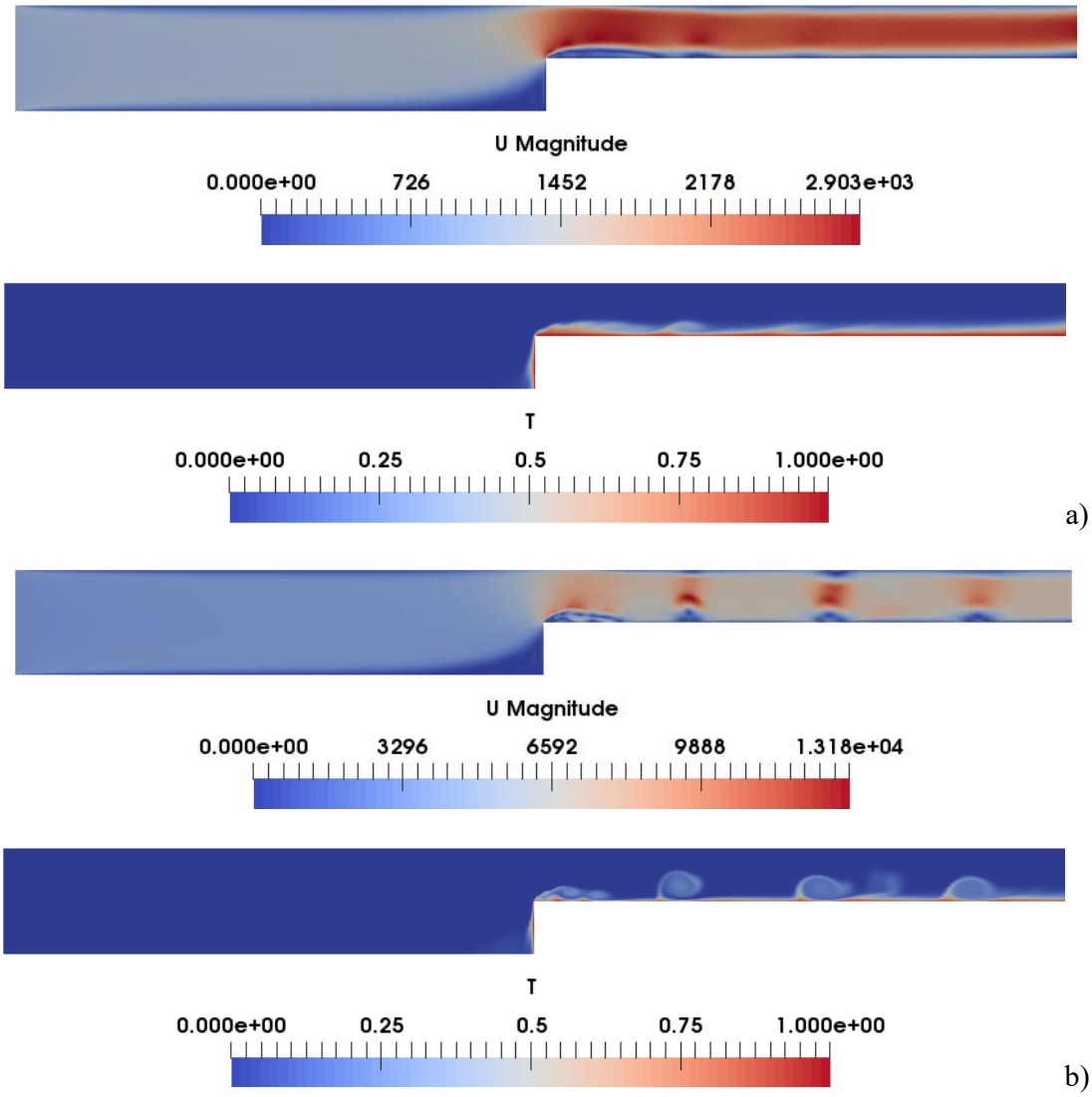

Figure 11: Snapshots of velocity field (left) and temperature distribution (right) for the case of hybrid forced/buoyancy convection (Ri=1), coaxial inflow and outflow sections and cavity with adiabatic bottom wall a) Ra=10^6, b) Ra=10^7. A bubble of recirculating flow originating from the leading edge (the step corner) can be seen in all cases.

Though its horizontal extension changes slightly in time, this zone always originates from the leading edge, i.e. the corner of the step. However, it is not the only recirculation region located on the top boundary of the step. Notably, for x>A/2 the kinematic boundary layer *separates and reattaches continuously* and, in light of the earlier results for larger values of the Richardson number, we argue that an explanation for this intermittent behavior should be sought in the temperature field**.** Plumes are located at those specific points where the flow is seen to be rising. Plume formation forces the fluid to rise and as result causes the fluid to separate from the horizontal wall of the hot step. However, the flow *re-attaches quickly* (the small space that is left behind on the surface can be viewed as a *bump*). Put simply, the plumes formed in this case do not have enough time to extend in the vertical direction as the imposed horizontal flow continuously bends them. As evident in Fig. 11b, while plumes are transported by the dominant flow in the downstream direction, they can give rise to some fascinating spiral-like configurations .

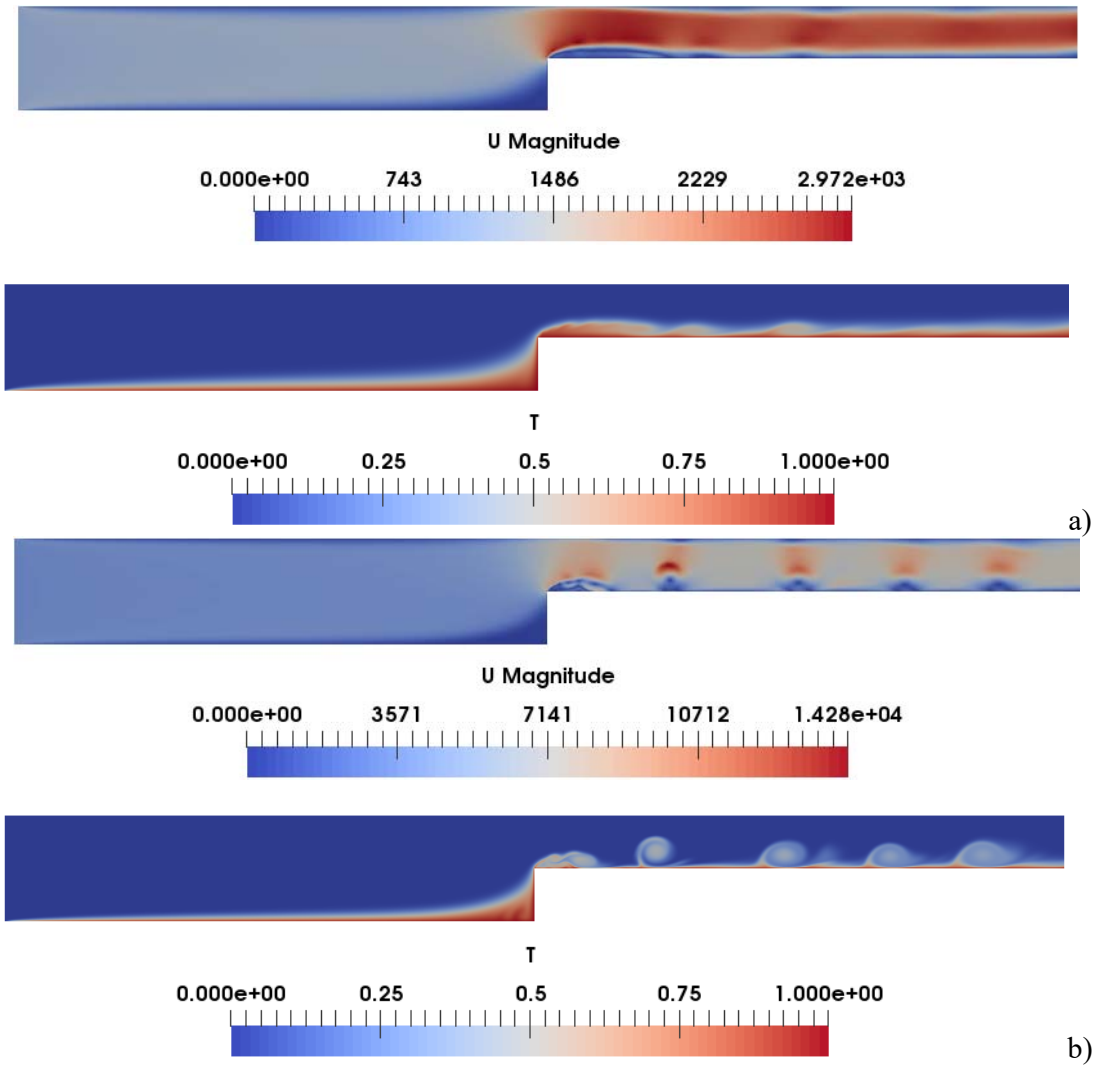

Figure 12: Snapshots of velocity field (left) and temperature distribution (right) for the case of hybrid forced/buoyancy convection (*Ri*=1), coaxial inflow and outflow sections and cavity with hot bottom wall: a) $Ra=10^6$, b) $Ra=10^7$. A bubble of recirculating flow originating from the leading edge (the step corner) can be seen in all cases.

Figure 12 refers to the other case in which the floor is kept at a constant temperature.
The most striking change with respect to the situations with larger values of the Richardson number (see again Fig. 8) essentially concerns the pre-step area, i.e. the region with x<A/2. Remarkably, for *Ri*=1 no bulges or *corrugation* of the thermal boundary layer can be detected in the left part of the domain even if the largest possible value of the Rayleigh number is considered ($Ra=10^7$ in Fig. 12b), which means that the boundary layer is essentially stable from a fluid-dynamic point of view in the considered range of *Ra*.

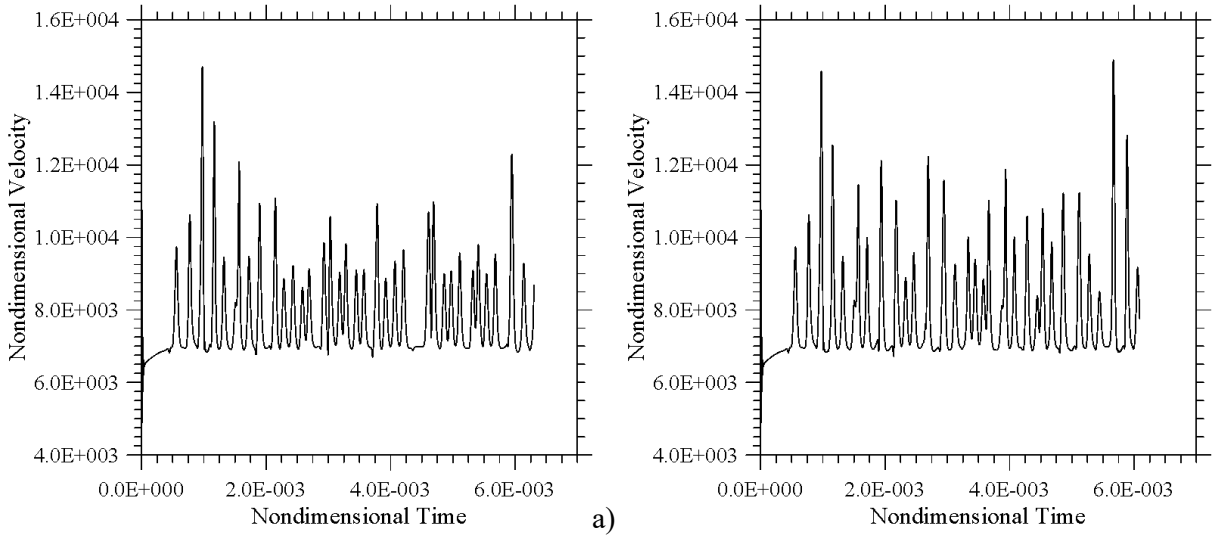

Figure 13: Velocity signals for *Ri* =1 and $Ra=10^7$ provided by a probe located in the region with reduced cross-sectional area (7.5, 0.75): a) adiabatic floor case ($\omega\cong3.58\text{x}10^4$), b) hot floor case ($\omega\cong3.38\text{x}10^4$).

The velocity plot for $Ra=10^7$ (Fig. 13) however shows that the flow is highly unsteady in the region located above the step, where the complex interplay between thermal plumes responsible for *vertical* fluid motion and the *horizontal* forced flow results again in a series of "bubbles" (localized regions of vorticity) more or less uniformly spaced along the boundary (which travel continuously in the downstream direction; the behavior being similar to that observed for the adiabatic floor case). Since a bubble of recirculating flow steadily attached to (originating from) the leading edge of the step can be seen in all cases, we come to the conclusion that hydrodynamic effects play a much important role in these cases, i.e. when relatively small (unit) values of the Richardson number are considered (the primary source of disturbances, which for larger values of *Ri* is represented by the relatively strong thermal plume stemming from the step corner is gradually transferred to a strongly unsteady bubble of hydrodynamic nature located in the same area; we will elaborate further this concept in Sect. 4).
As already discussed to a certain extent before, however, bubbles are also present along the entire extension of the top surface of the step. On the basis of the present framework, relying on direct

comparison of the statistics of the temporally evolving velocity field with the corresponding temperature field, we argue that these bubbles should be simply seen as the limiting condition attained by thermal plumes *folding in on themselves due to the fluid coming from the left*. As shown by both Fig. 11b and 12b, regardless of the specific thermal condition used for the floor of the duct, their appearance in space is surprisingly ordered (flow eruptions being created at periodic intervals), this observation being also supported by the regularity of the corresponding velocity fluctuations measured in a fixed point (Fig. 13).

4. Discussion

In this section some general arguments are elaborated to interpret the trends displayed by the considered system. In particular, such a discussion is supported by the precise determination of *the conditions for the onset of the first Hopf bifurcation* (namely, the critical Rayleigh number to be exceeded to produce oscillatory flow for different values of *Ri*). We intentionally use these data and the structure of the related fluid-dynamic "disturbances" to get additional insights into the mechanisms that govern the onset of unsteadiness and the ensuing evolution towards chaos.
We wish to remark that, given the nature of the numerical strategy used in the present study (relying on the direct solution of the balance equations for mass, momentum and energy in their complete, time-dependent and non-linear form, as illustrated in Sect. 2), the transition *Ra* has been determined by means of numerical experiments (by increasing it until the flow becomes oscillatory and then increasing/decreasing it in a certain neighbor of the previously found value). The final value has been determined through extrapolation to zero of the amplitude of oscillations. Moreover, the spatial structure of the fluid-dynamic disturbances responsible for the transition from steady to oscillatory flow has been determined 'a posteriori', i.e. by subtracting the time-averaged thermofluid-dynamic field to the instantaneous one for conditions located slightly above the transition point (i.e. *Ra* slightly larger than Ra_{cr}).
Towards the end to elaborate an exhaustive picture of the overall thermofluid-dynamic scenario, we also discuss the quantitative data obtained for the heat exchange taking place between the fluid and the wall of the heated step (i.e. its vertical and horizontal boundaries) for the different situations examined in Sect. 3. For the convenience of the Reader, all this information is organized in the form of synthetic tables and 'maps' where the critical conditions and the Nusselt number are reported as function of *Ra* and *Ri*.

4.1 Influence of the Richardson number on the bifurcation scenario

The bifurcation scenario for the system with adiabatic floor is presented in Fig. 14. Snapshots of the related disturbances have been collected in Fig. 15.

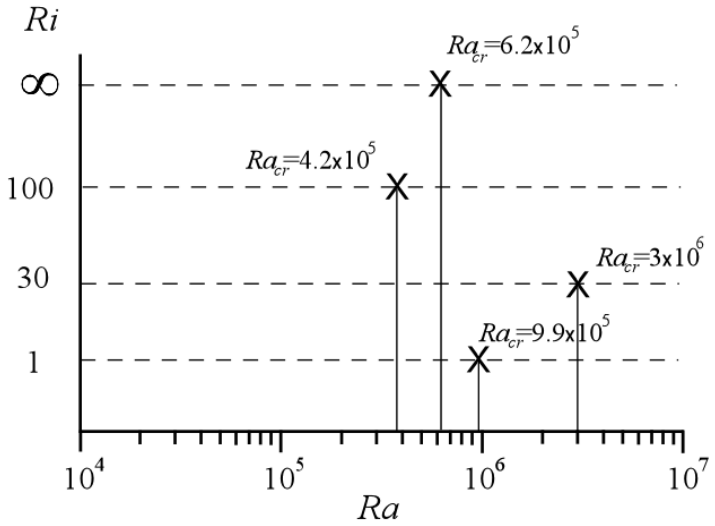

Figure 14: Bifurcation scenario for the adiabatic floor case.

On the basis of the numerical results shown in Figs. 3, it could have already been concluded that for pure buoyancy with the adiabatic floor the transition from stationary to oscillatory conditions occurs somewhere between $Ra = 10^5$ and $Ra = 10^6$. By means of an extensive parametric investigation conducted by refining iteratively the value of the Rayleigh number in this interval, we could determine the value of Ra required for the Hopf bifurcation as $Ra_{cr} \cong 6.2 \times 10^5$ (see the line corresponding to $Ri \to \infty$ in Fig. 14).

A snapshot of the related disturbances (obtained by subtracting the time-averaged velocity field from the instantaneous one) is shown in Fig. 15a. This figure is instrumental in showing that the perturbations behave essentially as a wave traveling to the left region of the domain (using the upper branch of the Hadley circulation as a *substrate for propagation* as explained in Sect. 3). This wave apparently originates from the rolls of RB nature located above the step in proximity to the corner ($A/2<x<3A/4$). Accordingly, we argue that the main source of the instability is located just above the step, in the area where the coalescence between the main Hadley circulation and the first roll of the RB series occurs. This observation, in turn, indicates that the transition process is essentially driven by a *competition of the RB and Hadley mechanisms* in a very localized region. The existence of a wave travelling towards the left (visible in the left part of the cavity) should therefore be seen as a *secondary effect* induced by such a process. Put simply, the interplay of RB and Hadley flow in proximity to the corner is the main oscillatory mechanism that produces a local 'forcing' able to excite a shear-driven wave travelling in the left part of the cavity (where the Hadley flow is dominant). Mechanisms of such a kind have been extensively observed in purely Hadley flow problems (buoyancy convection in rectangular containers heated from the side, Le Quéré and Behnia [75] where the forcing needed for the excitation the wave is generally provided by boundary layer instabilities or similar phenomena (Ferialdi et al. [76], Gelfgat [3, 4]).

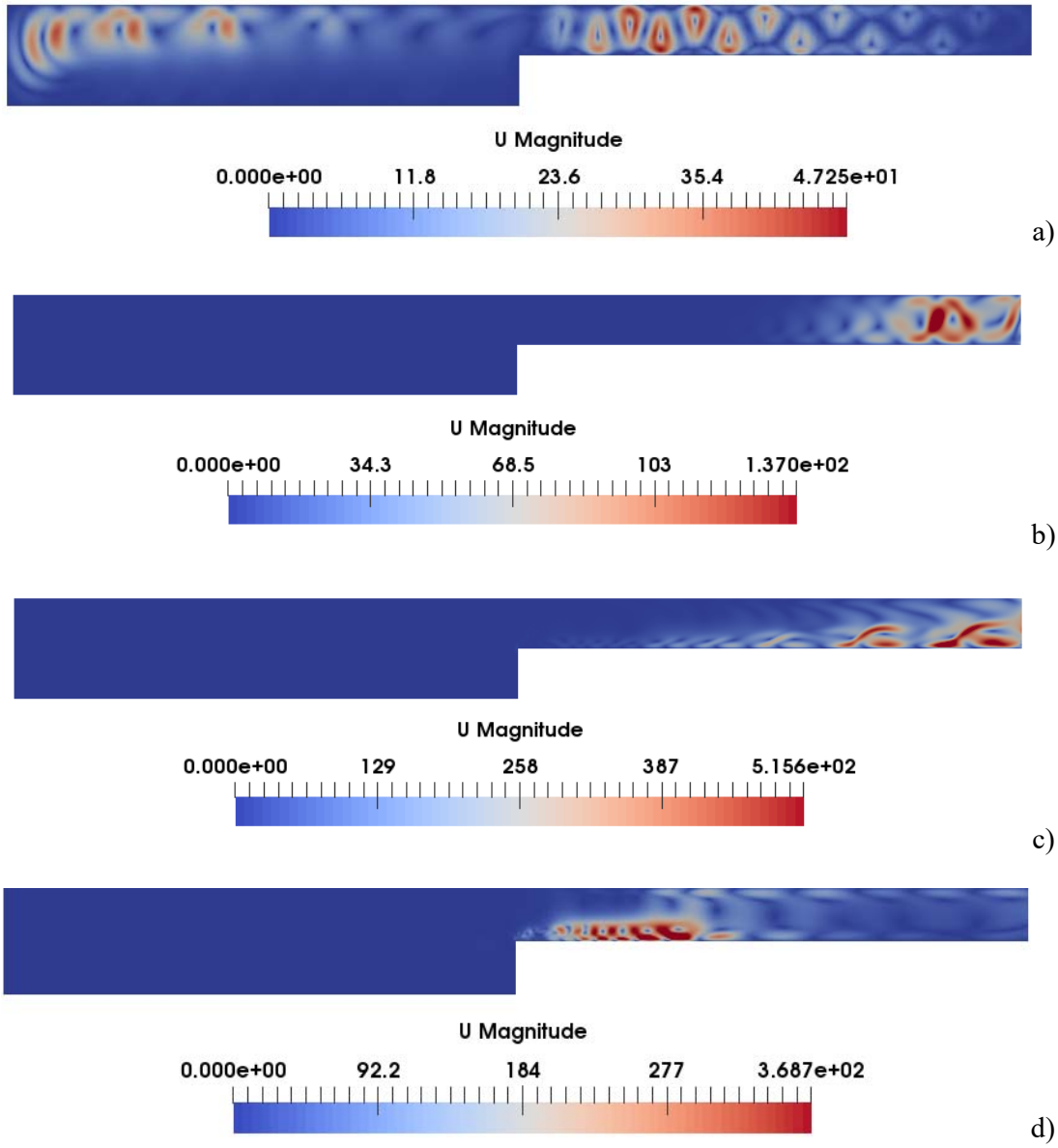

Figure 15: Snapshot of the velocity disturbances for the cavity with the adiabatic floor (first Hopf bifurcation), a) $Ri \to \infty$, $Ra \cong 6.6 \times 10^5$, b) $Ri=100$, $Ra \cong 4.3 \times 10^5$, c) $Ri=30$, $Ra \cong 4 \times 10^6$, d) $Ri=1$, $Ra \cong 1 \times 10^6$.

For $Ri=100$, (Fig. 14, second line from the top) the value of the critical Rayleigh number decreases appreciably with respect to that obtained in the limit as $Ri \to \infty$. Remarkable changes can also be seen in the mechanism underpinning the instability (as revealed by Fig. 15b). The disturbances still manifest themselves in the form of a wave. The location and sense of propagation of this wave, however, are completely different. It is now located in the right part of the domain (the region x>A/2 with reduced cross-sectional extension). Moreover, the disturbances travel in the downstream direction with respect to the forced flow, i.e. from left to right (it was in the opposite sense for $Ri \to \infty$).

The key to understanding this behavior lies in considering the competition between convection of the RB type and forced flow. While the former tends to create localized eruptions of hot fluid directed upwards (thermal plumes), the latter tends to displace fluid in the horizontal direction. The instability is essentially a result of the interplay of these two concurrent convective mechanisms along the entire top surface of the step.

A further decrease in the Richardson number (*Ri*=30), make obviously the contribution brought in by forced convection more important. This is indeed reflected by the morphology of disturbances. As a fleeting glimpse into Fig. 15c would confirm, λ-shaped disturbances essentially develop *inside the thermal and kinematic boundary layers* (which for Pr=1 have obviously comparable thickness). The required value of the Rayleigh number undergoes a significant increase, and a justification for this behavior can be rooted directly in the nature of the disturbances per se (which, unlike those shown in Fig. 15b, are now forced to grow inside the boundary layer).

Figure 15d is extremely useful as it reveals that the main mechanism responsible for the development of unsteady flow is transferred from that associated with the propagation and growth of disturbances in the boundary layer for *Ri*=30, to a different process where disturbances are essentially produced inside the recirculating bubble of limited extension, which originates from the leading edge for *Ri*=1.

As a concluding remark for this analysis, we wish to highlight that the continuous switch from one instability mechanism to another as the Richardson number is varied should be regarded as a relevant justification for the scattered appearance of the critical points in Fig. 14.

The distribution of critical parameters for the companion configuration with the hot floor is illustrated in Fig. 16.

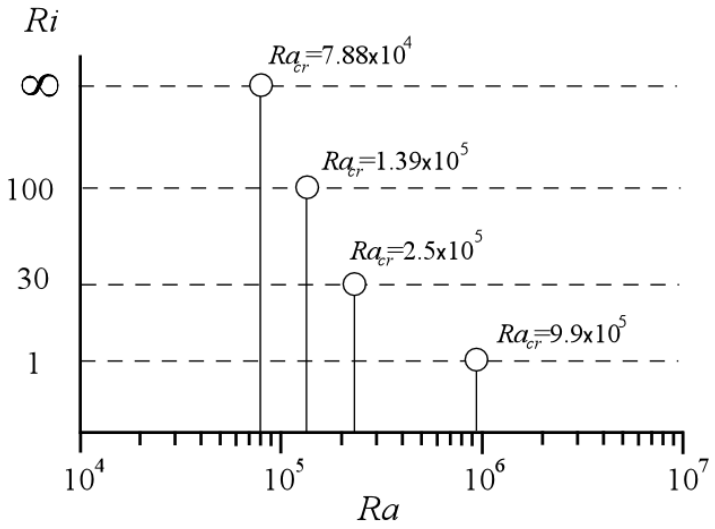

Figure 16: Bifurcation scenario for the hot floor case.

This figure and the companion sequence of fluid-dynamic disturbance snapshots collected in Fig. 17 indicate that interpreting the role played in such dynamics by the thermal conditions adopted for the floor (x<A/2) is not as straightforward as one would imagine.

As implicitly evident in Fig. 16, the instability scenario dramatically changes. As already indicated by the preliminary analysis (Sect. 3.1) conducted by progressively increasing the order of magnitude of the Rayleigh number, the transition to oscillatory flow for pure buoyancy flow ($Ri \to \infty$) takes place earlier for the hot floor in comparison to the adiabatic case (for a smaller Ra, i.e. $Ra_{cr} \cong 7.88 \times 10^4$, determined using the same approach discussed before, see the line of Fig. 16 corresponding to $Ri \to \infty$). A striking difference can be spotted when the spatial structure of the related disturbances is considered (Fig. 17a). Fluid-dynamic perturbations keep on originating from the corner of the step as a result of the significant amount of vertical shear produced by the inclined thermal plume located there (as shown in Fig. 6 this plume is always inclined to the left). In this case, however, no wave traveling to the left is generated owing to the lack of a horizontal current of the Hadley type which can support it.

An explanation for the decrease in the value of the critical Rayleigh number with respect to the equivalent configuration with the adiabatic floor can be elaborated in its simplest form on the basis of the argument that the system is entirely dominated (over its entire horizontal extension) by pure RB convection. This leads to a significant *increase in the strength of the main thermal plume* originating from the corner of the step and in the ensuing associated shear stress (responsible for the onset of the oscillatory instability, [77-80]).

As revealed by Fig. 17b (Ri=100), if a forced flow is superimposed on thermal convection, the disturbances generated by the corner plume (which changes its inclination in order to align with the forced flow) are transported in the downstream direction, thereby exciting a response that develops in the form of weak rolls superimposed on the horizontal current (it can be seen that the amplitude of this disturbance is amplified as it travels towards the outlet).

Interestingly, as quantitatively substantiated by the data reported in Fig. 16, a decrease in Ri has in general a beneficial effect in terms of critical Rayleigh number, i.e. Ra_{cr} becomes higher (the trend is monotonic). In other words, the presence of forced flow has a *stabilizing effect* on the overall dynamics, which requires a proper interpretation too.

The reader could be led to a heuristic realization of the related underlying cause-and-effect relationship by simply considering that, as already explained to a certain extent in the previous text, the instability of mixed forced-buoyancy convection is essentially driven by the competition of these two different mechanisms of convection. The tendency of hot fluid to rise vertically and the effect of the imposed horizontal flow that tends to bend it to the right (eventually causing the reattachment of the boundary layer) is the main mechanism leading to the unsteady production of vorticity in the form of "bubbles" which travel in the downstream direction. A decrease in Ri, i.e. an increase in the relative importance of forced flow with respect to thermal buoyancy, must necessarily correspond to higher values of the Rayleigh number needed to *excite the competition of buoyant and forced flow in the duct*.

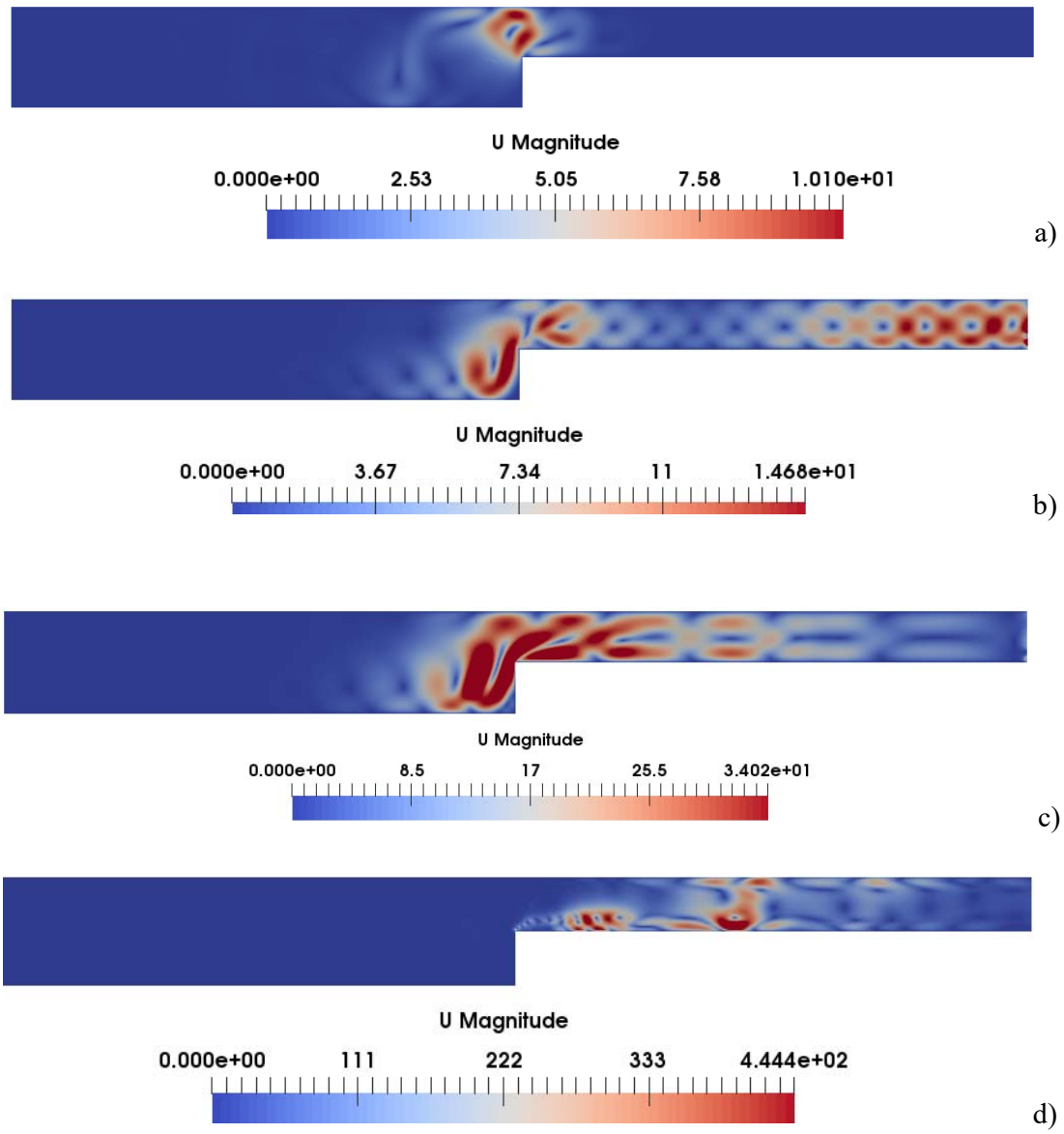

Figure 17: Snapshot of the velocity disturbances for the cavity with the hot floor, (first Hopf bifurcation), a) $Ri \to \infty$, $Ra \cong 7.89 \times 10^4$, b) $Ri=100$, $Ra \cong 1.5 \times 10^5$, c) $Ri=30$, $Ra \cong 3 \times 10^5$, d) $Ri=1$, $Ra \cong 1 \times 10^6$.

As witnessed by Fig. 17c, as Ri is decreased from 100 to 30, there is a small variation in the required value of the Rayleigh number and disturbances still take their energy from the main plume that originates from the leading edge. Comparison with the equivalent case with the adiabatic floor (Fig. 15c), indicates that the much higher value of Ra_{cr} in that case is due to the lack of the strong thermal plume located at x≅A/2 (among other things, this observation also provides a justification for the different level of complexity displayed by the signals in the left and right panels of Fig. 10; the more complex spectrum for the hot floor case is obviously due to the two orders of magnitude of distance between Ra=10^7 and the Ra_{cr}).

For *Ri*=1, the corner plume finally collapses in a region of recirculating flow attached to the leading edge, thereby making the main instability mechanism for the hot floor case equivalent to that already discussed for the adiabatic floor configuration (as also indirectly confirmed by the fact that the critical Rayleigh number is essentially the same). Another way to think about this behavior is to consider that for such circumstances the dynamics produced by buoyancy convection in the pre-step area (x<A/2) have an almost negligible influence on the mechanisms supporting the instability (which further confirms our interpretation about the more important role played by hydrodynamic disturbances in this case).

4.2 Heat Exchange

With the only exception of the purely diffusive state, in general, for the adiabatic floor configuration $Nu_{step}^{vert} > Nu_{step}^{horiz}$ (Table VII). This result is not unexpected. For the case of pure buoyancy convection, a simple rationale for this behavior can be elaborated taking into account the relative importance (or magnitude) of the buoyancy forces at work in the left (x<A/2) and right (x>A/2) regions of the physical domain. As the intensity of this force is known to scale with L^3 where L is the effective depth of the considered region, this fundamental dependence is the key ingredient needed to formulate a justification for the different magnitude of the Nusselt number related to the two sides of the step. Under a slightly different perspective, the same concept could be re-introduced basing it directly on the 'effective' Rayleigh number experienced by the fluid in the two sides of the cavity (that affecting the fluid located in the region x>A/2 being eight times smaller than that effective for x<A/2). Put simply, as the vertical side "feels" the strong convective cell of the Hadley type established in the left portion of the domain, the intensity of heat exchange along this wall will obviously be higher (while the horizontal side is only subjected to the weak rolls of the RB type emerging there).

A similar argument holds when finite values of the Richardson number are considered (though this case calls for a complementary explanation). For such a situation, for a given value of the Rayleigh number the velocity of fluid rising along the vertical side of the step is even higher than that produced for pure buoyancy convection. Such an increase in velocity obviously follows from the presence of two concurrent mechanisms driving the fluid along the vertical wall, namely, the buoyancy effect (which forces fluid to rise) and the additional upward velocity produced by the imposed flow (which forces fluid to turn around the step). Therefore, the reason for the even larger difference between Nu_{step}^{vert} and Nu_{step}^{horiz} when the values Ri = 30 and =100 are considered resides in the presence of these two aiding (reciprocally reinforcing) effects.

Table VII: Nusselt number as a function *Ra* and *Ri* for the adiabatic floor case.

Ra	*Ri*	Nu_{step}^{horiz}	Nu_{step}^{vert}	Regime
0	N/A	2.0417	1.6731	Purely Diffusive
10^4	∞	2.0077	4.6240	Steady
10^5	-	5.6375	9.4742	Steady
10^6	-	9.8594 (average)	17.5227 (average)	Quasi-periodic
10^7	-	16.5836 (average)	30.9278 (average)	Moderately Turbulent
10^4	100	1.2987	5.6315	Steady
10^5	-	3.2347	10.6367	Steady
10^6	-	6.3597(average)	19.7056 (average)	Multi-frequency spectrum
10^7	-	16.5881(average)	35.8678(average)	Moderately Turbulent
10^4	30	2.2856	5.8999	Steady
10^5	-	4.1605	10.8647	Steady
10^6	-	6.1746 (average)	20.0669(average)	Steady
10^7	-	13.1961 (average)	36.3426 (average)	Time-periodic
10^4	1	5.1047	9.2652	Steady
10^5	-	7.6590	15.6639	Steady
10^6	-	12.7710 (average)	26.4171 (average)	Quasi-Periodic
10^7	-	39.07695 (average)	45.4150 (average)	Unsteady with dominant frequency

Table VIII: Nusselt number as a function *Ra* and *Ri* for the hot floor case.

Ra	*Ri*	Nu_{step}^{horiz}	Nu_{step}^{vert}	Regime
0	N/A	2.0329	0.8782	Purely Diffusive
10^4	∞	2.0113	0.9457	Steady
10^5	-	5.6299	1.6408	Periodic
10^6	-	10.8293 (average)	3.0102 (average)	Periodic
10^7	-	18.6177 (average)	8.0191 (average)	Weakly Turbulent
10^4	100	0.2390	0.3284	Steady
10^5	-	1.4868	2.0256	Steady
10^6	-	5.5144 (average)	7.1233 (average)	Multifrequency
10^7	-	14.2736 (average)	19.5536 (average)	Moderately Turbulent

10^4	30	1.0157	0.9922	Steady
10^5	-	2.6784	2.7333	Steady
10^6	-	6.1050 (average)	8.2020 (average)	Multifrequency
10^7	-	16.1624 (average)	24.7982 (average)	Moderately Turbulent
10^4	1	3.6248	2.5971	Steady
10^5	-	5.4746	4.8390	Steady
10^6	-	10.2654 (average)	8.9180 (average)	Quasi-Periodic
10^7	-	38.1026 (average)	16.5762 (average)	Unsteady with dominant frequency

The data for the companion case with hot floor are quantitatively presented in Table VIII. Careful comparison with Table VII reveals a significant *lowering* of Nu_{step}^{vert}, which requires a proper justification.

In particular, a straightforward interpretation can be sought directly in the temperature distribution. In this regard, coming back to the results shown in Figs. 6, 8 and 12 is extremely useful; once again, these figures clearly show the presence of well-defined thermal (hot) boundary layers developing along the (hot) horizontal floor of the duct. To emphasize further the significance of this observation, one should keep in mind that, unlike the configuration with the adiabatic bottom (where all the fluid transported towards the step is cold), for these cases, fluid that has already acquired a significant amount of heat tends to be entrained into the boundary layer developing along the vertical step wall. The reduced temperature difference between the incoming fluid and the temperature of the step itself can obviously be regarded as the main factor contributing to the generalized observable shrinkage in the values of Nu_{step}^{vert}.

5. Conclusions

The main conclusions of the present study can be summarized as follows:

- When the floor of the region preceding the step is adiabatic a change from the condition Ri=∞ to finite Ri causes a dramatic variation in the system oscillatory response and related patterning behavior. While for pure buoyancy the Hopf bifurcation must be ascribed to an instability of the leftward directed current of the Hadley type originating from the step corner, for finite Ri=100, it manifests in the form of plumes that periodically nucleate at a certain distance (in the downstream direction) from the step corner and travel to the right.
- An increase in *Ra* at fixed *Ri* (yet for the thermally insulated floor) has a very interesting effect. Plumes are produced at a much smaller distance from the leading edge. Moreover, their extension in the vertical direction becomes progressively smaller, which can be interpreted taking into account the dual influence of a simultaneous increase of *Ra* and Re

(the former contributing to make plume caps smaller, the latter reducing the available time for their stem to grow before they leave the domain through the outflow section).

- Regardless of the considered thermal condition for the floor preceding the step, when turbulent conditions are attained the overall frequency spectrum is shifted to the right with respect to the case of pure buoyancy, i.e. for Ri=100 the energy tends to reside on smaller temporal scales (which indicates that new instability mechanisms are enabled with respect to the situation with pure buoyancy convection).
- A decrease in Ri (Ri=30), forces the disturbances to develop inside the thermal and kinematic boundary layers (which for Pr=1 have the same thickness).
- When the Richardson number is finally reduced to 1, the primary source of disturbances, which for larger values of Ri is represented by the relatively strong thermal plume originating from the step corner is gradually transferred to a strongly unsteady bubble located in the same area; hydrodynamic effects play a much important role in these cases; the kinematic boundary layer along the upper surface of the step separates and reattaches continuously (due to plumes being continuously formed and the imposed horizontal flow that quickly bends them).
- Another outcome of the focused comparison of the fundamental situations with adiabatic and bottom floors is that the dynamics of the boundary layer established along the vertical side of the step can play a crucial role in determining the heat exchange in this region.
- For the adiabatic floor case, the vigorous upward fluid motion is responsible for the higher values taken by the Nusselt number along the vertical wall (with respect to the corresponding value for the horizontal side of the step).
- When the bottom wall of the duct is kept at fixed hot temperature, the additional heat entrained into the vertical boundary layer is the main reason for which Nu_{step}^{vert} undergoes an appreciable decrease.

As an additional concluding remark, we would like to point out that, although, as illustrated above, useful generalizations can be built using the main outcomes of two-dimensional numerical simulations (which allow much more efficient exploration of the space of parameters), future studies shall be devoted to overcome this constraint and tackle more realistic 3D configurations. As the required number of high-fidelity evaluations, however, would become impractical (if wide ranges of the controlling parameters like those examined in the present study were considered), there is therefore a strong need to adopt alternate strategies. These could be based on suitable turbulence models by which the inherently chaotic behavior displayed by these systems in certain regions of the space of parameters (as indicated by the present study) is properly captured without resorting to computationally prohibitive grid densities. This may be seen as a spur to continue the line of inquiry initiated in the present work (which given the absence of relevant information to properly constrain the 'parameters' needed by turbulence models has been initially limited to 2D flow).

Acknowledgements

The authors would like to thank Alessio Boaro for performing the additional simulations presented in Sect. 2.5 using the ANSYS Fluent computational platform.

References

[01] Plant R.D. and Saghir S., (2021), "Numerical and experimental investigation of high concentration aqueous alumina nanofluids in a two and three channel heat exchanger", *International Journal of Thermofluids*, 9, 100055.

[02] Skinner S.N. and Behtash H. Z., (2017), "Semi-span wind tunnel testing without conventional peniche"*, Experiments in Fluids*, 58(12), 163.

[03] Gelfgat A. Yu., (2020), "Instability of natural convection of air in a laterally heated cube with perfectly insulated horizontal boundaries and perfectly conducting spanwise boundaries", *Phys. Rev. Fluids* 5, 093901

[04] Gelfgat A. Yu., (2020), "Instability of natural convection in a laterally heated cube with perfectly conducting horizontal boundaries", *Theoretical and Computational Fluid Dynamics*, 34, 693–711.

[05] Brottier L. and Bennacer R., (2020), "Thermal performance analysis of 28 PVT solar domestic hot water installations in Western Europe", *Renewable Energy*, 160, pp. 196-210

[06] Souissi F., Guellouz M.S., Ben Salah N. , Kaddeche S., (2020), "The flow structure in the narrow gaps of compound channels: a linear stability analysis", *International Journal of Computational Fluid Dynamics*, 2020, 34(1), 14-24.

[07] Molochnikov V. M., Mazo A. B., Kalinin E. I., Malyukov A. V., Okhotnikov D. I., and Dushina O. A., (2019), "Formation and turbulent breakdown of large-scale vertical structures behind an obstacle in a channel at moderate Reynolds numbers," *Phys. Fluids* 31, 104104.

[08] Hattori H. and Nagano Y., (2010), "Investigation of turbulent boundary layer over forward facing step via direct numerical simulation", *Int. J. Heat Fluid Flow*, 31, 284-294.

[09] Dai Z., Li T., Zhang W., Zhang J., (2020), "Numerical Study on Aerodynamic Performance of High-Speed Pantograph with Double Strips", *Fluid Dynamics & Materials Processing*, 16 (1), 31-40.

[10] Redchyts D.O., Shkvar E.A., Moiseienko S.V., (2020), "Computational Simulation of Turbulent Flow Around Tractor-Trailers", *Fluid Dynamics & Materials Processing*, 16(1), 91-103.

[11] Sherry M., Jacono D.L., Sheridan J., (2010), "An experimental investigation of the recirculation zone formed downstream of a forward facing step", *J. Wind Eng. Ind. Aerod.*, 98, 888-894.

[12] Hillier R. and Cherry N., (1981), "The effects of stream turbulence on separation bubbles", *Journal of Wind Engineering and Industrial Aerodynamics* 8, 49–58.

[13] Houde H., Lu J. and Bao W., (1994), "A Discrete Artificial Boundary Condition for Steady Incompressible Viscous Flows in a No-Slip Channel Using a Fast Iterative Method", *J. Comput. Phys*., 114, 201–208.

[14] Stüer H., Gyr A., Kinzelbach W., (1999), "Laminar separation on a forward facing step", *Eur. J. Mech. B/Fluids* 18, 675–692.

[15] Barbosa-Saldaña J.G. and Anand N. K., (2007), "Flow Over a Three-Dimensional Horizontal Forward-Facing Step", *Numerical Heat Transfer, Part A: Applications*, 53(1),1-17.

[16] Abdalla I. E., Yang Z. and Cook M., (2009), "Computational analysis and flow structure of a transitional separated-reattached flow over a surface mounted obstacle and a forward-facing step", *International Journal of Computational Fluid Dynamics*, 23(1), 25-57, DOI: 10.1080/10618560802566246

[17] Zhu H. and Fu S., (2017), "Forward-facing steps induced transition in a subsonic boundary layer", Science China, Physics, Mechanics & Astronomy, 60(10): 104712

[18] Graziani A., Lipperta M., Uystepruyst D., Keirsbulck L., (2017), "Scaling and flow dependencies over forward-facing steps", *International Journal of Heat and Fluid Flow* 67, 220–229
[19] Kiya M. and Sasaki K., (1983), "Structure of a turbulent separation bubble", *J. Fluid Mech.*, 137, 83–113.
[20] Cherry N.J., Hillier R., Latour M.E., (1985), "Unsteady measurements in a separated and reattaching flow", *J. Fluid Mech.* 144, 13–46 .
[21] Largeau J.F. and Moriniere V., (2007), "Wall pressure fluctuations and topology in separated flows over a forward-facing step", *Exp Fluids*, 42, 21-40.
[22] Abu-Mulaweh H.I., Armaly B.F., Chen T.S., (1993), "Measurements of laminar mixed convection flow over a horizontal forward-facing step", *J. Thermophys. Heat Transfer,* 7, 569–573.
[23] Abu-Mulaweh H.I., (2003), "A review of research on laminar mixed convection flow over backward- and forward-facing steps", *Int. J. Therm. Sci.*, 42(9), 897–909.
[24] Moosavi R. and Nassab A.G., (2008), "Turbulent forced convection over a single inclined forward step in a duct: part I-flow field", *Eng Appl Comp Fluid*, 2, 366-374.
[25] Nassab S.A.G., Moosavi R., Sarvari S.M.H., (2009), "Turbulent forced convection flow adjacent to inclined forward step in a duct", *Int. J. Therm. Sci.*, 48, 1319-1326.
[26] Oztop H.F., Mushatet K. S., Yılmaz İ., (2012), "Analysis of turbulent flow and heat transfer over a double forward facing step with obstacles", *International Communications in Heat and Mass Transfer*, 39,1395–1403.
[27] Xie W.A. and Xi G.N., (2017), "Geometry effect on flow fluctuation and heat transfer in unsteady forced convection over backward and forward facing steps", *Energy,* 132, 49–56.
[28] Liou T. M., Hwang J. J., and Chen S. H., (1993), "Simulation and measurement of enhanced turbulent heat transfer in a channel with periodic ribs on one principal wall," *Int. J. Heat Mass Transfer* 36(2), 507–517.
[29] Miyake Y., Tsujimoto K., and Nakaji M., (2001), "Direct numerical simulation of roughwall heat transfer in a turbulent channel flow," *Int. J. Heat Fluid Flow* 22, 237–244.
[30] Miyake Y., Tsujimoto K., and Nakaji M., (2002) "Numerical simulation of channel flow with a rib-roughened wall," *J. Turbul*. 3, N35.
[31] Chandra P. R., Alexander C. R., and Han J. C., (2003), "Heat transfer and friction behaviors in rectangular channels with varying number of ribbed walls," *Int. J. Heat Mass Transfer* 46, 481–495.
[32] Peng W., Jiang P. X., Wang Y. P., and Wei B. Y., (2011), "Experimental and numerical investigation of convection heat transfer in channels with different types of ribs," *Appl. Therm. Eng.* 31, 2702–2708.
[33] Fouladi F., Henshaw P., Ting D. S.-K., and Ray S., (2017), "Flat plate convection heat transfer enhancement via a square rib," *Int. J. Heat Mass Transfer* 104, 1202–1216.
[34] Sun Z. and Jaluria Y., (2011), "Conjugate thermal transport in gas flow in long rectangular microchannel", *J. Electron. Packag*. 133(2), 021008 (11 pages).
[35] Arrif T.,, Chehhat A., Abo-Serie E., Benchabane A., (2018), "Numerical Study of Natural Convection in Square Tilted Solar Cavity Considering Extended Domain", *Fluid Dynamics & Materials Processing*, 14(4), 223-242.
[36] Nadjib H., Adel S., Djamel S., Abderrahmane D., (2018), "Numerical Investigation of Combined Surface Radiation and Free Convection in a Square Enclosure with an Inside Finned Heater", *Fluid Dynamics & Materials Processing*, 14(3), 155-175.
[37] Lappa M., (2019), "On the Highly Unsteady Dynamics of Multiple Thermal Buoyant Jets in Cross Flows", *Phys. Fluids*, 31, 115105 (27 pages).
[38] Lappa M. and Inam S., (2020), "Thermogravitational and hybrid convection in an obstructed compact cavity", *Int. J. Thermal Science*, 156, 106478 (21 pages).
[39] Lappa M., (2017), "On the oscillatory hydrodynamic modes in liquid metal layers with an obstruction located on the bottom", *Int. J. Therm. Sci.*, 118, 303–319. DOI: 10.1016/j.ijthermalsci.2017.04.013

[40] Lappa M., (2019a), "On the gravitational suppression of hydrothermal modes in liquid layers with a blockage on the bottom wall", *Int. J. Therm. Sci.*, , 145, November 2019, 105987 (19 pages)
[41] Lappa M., (2019b), "A mathematical and numerical framework for the simulation of oscillatory buoyancy and Marangoni convection in rectangular cavities with variable cross section", Chapter 12 (pp. 419-458) in *Computational Modeling of Bifurcations and Instabilities in Fluid Mechanics* (Springer Mathematical Series, 2018, Part of the Computational Methods in Applied Sciences book series - COMPUTMETHODS, volume 50), Editor Alexander Gelfgat - ISBN 978-3-319-91493-0. DOI: 10.1007/978-3-319-91494-7
[42] Khatra L., El Qarnia H., El Ganaoui M., (2019), "The Effect of the Fin Length on the Solidification Process in a Rectangular Enclosure with Internal Fins", *Fluid Dynamics & Materials Processing*, 15(2), 125-137.
[43] Yarin L.P., (2009) Cooling Systems of Electronic Devices. In: Fluid Flow, Heat Transfer and Boiling in Micro-Channels. Heat and Mass Transfer. Springer, Berlin, Heidelberg
[44] Venkatasubbaiah K. and Jaluria Y., (2012), "Numerical simulation of enclosure fires with horizontal vents", *Numer. Heat Tran.* 62, 179–196.
[45] Morsli S., Boussoufi M., Sabeur A., El Ganaoui M., Bennacer R., (2018) "Small to large scale mixed turbulent convection: buildings application", *Int. J. Numer. Methods Heat Fluid Flow*, 28(1), 188-205, https://doi.org/10.1108/HFF-10-2017-0392
[46] Kachi S., Bensouici F.Z., Ferroudj N. and Boudebous S., (2019), "Effect of Richardson Number on Unsteady Mixed Convection in a Square Cavity Partially Heated From Below", *Fluid Dynamics & Materials Processing*, 15(2), 89-105. doi:10.32604/fdmp.2019.00263
[47] Daniels P.G., (1984), "Roll-pattern evolution in finite-amplitude Rayleigh-Bénard convection in a two-dimensional fluid-layer bounded by distant sidewalls", J. *Fluid Mech*., 143: 125-152.
[48] Hart J.E., (1972), "Stability of thin non-rotating Hadley circulations",. *J. Atmos. Sci*., 29: 687-697.
[49] Lappa M., (2009), Thermal Convection: Patterns, Evolution and Stability, John Wiley & Sons, Ltd (2009, Chichester, England).
[50] Hattori T , Norris S , Kirkpatrick M , Armfield S., (2013), "Comparison of non-reflective boundary conditions for a free-rising turbulent axisymmetric plume", *Int. J. Numer. Methods Fluids*, 72(12), 1307–1320.
[51] Dong S., Karniadakis G.E., Chryssostomidis C., (2014), "A robust and accurate outflow boundary condition for incompressible flow simulations on severely-truncated unbounded domains", *J. Comput. Phys*., 261, 83–105.
[52] Issa R.I.,(1986), "Solution of the implicitly discretized fluid flow equations by operator-splitting", *J. Comp. Physics*, 62, 40-65.
[53] Ladyzhenskaya O.A., (1969), The Mathematical Theory of Viscous Incompressible Flow, Gordon and Breach, 2nd Edition, New York - London, 1969.
[54] Gresho P.M., Sani R.T., (1987), "On pressure boundary conditions for the incompressible Navier-Stokes equations", *Int. J. Numer. Meth. Fluids*, 7, 1111-1145.
[55] Guermond J.-L. and Quartapelle L., (1998), "On stability and convergence of projection methods based on pressure Poisson equation", *Int. J. Numer. Meth. Fluids*, 26, 1039-1053.
[56] Guermond J.-L., Minev P. and Shen J., (2006), "An Overview of Projection Methods for Incompressible Flows". Comput. Methods, *Comput. Methods Appl. Mech. Eng*., 195, 6011-6045.
[57] Lappa M., (1997), "Strategies for parallelizing the three-dimensional Navier-Stokes equations on the Cray T3E"; Science and Supercomputing at CINECA, 11, 326-340. ISBN-10: 88-86037-03-1, M. Voli, Editor (Bologna, Italy).
[58] Lappa M., (2016), "A Mathematical and Numerical Framework for the Analysis of Compressible Thermal Convection in Gases at very high Temperatures", *Journal of Computational Physics*, 313, 687–712.
[59] Rhie C.M. and Chow W.L., (1983), "Numerical study of the turbulent flow past an airfoil with trailing edge separation", *AIAA J* 21,1525–1532

[60] Ouertatani N., Cheikh N. B., Beya B.B., Lili T., (2008), "Numerical simulation of two-dimensional Rayleigh-Benard convection in an enclosure", *C.R. Mecanique*, 336(5), 464-470.
[61] De Vahl Davis and Jones I. P., (1983), "Natural convection in a square cavity a comparison exercise", *International journal for numerical methods in fluids*, vol. 3, pp. 227-248.
[62] Mizushima J. and Adachi T., (1997), "Sequential Transitions of the Thermal Convection in a Square Cavity", *J. Phys. Soc. Jpn*., 66(1): 79-90.
[63] Hutchinson B.R. and Raithby G.D., (1986), "A multigrid method based on the additive correction strategy", *Numer. Heat Transf*., 9, 511–537.
[64] Kolmogorov, A.N. (1941) "The local structure of turbulence in incompressible viscous fluids at very large Reynolds numbers", *Dokl. Akad. Nauk. SSSR* 30, 299-303. Reprinted in *Proc. R. Soc. London* A 434, 9-13 (1991).
[65] Kolmogorov, A.N. (1941) "Dissipation of energy in isotropic turbulence", *Dokl. Akad. Nauk. SSSR*, 32, 19-21.
[66] Kraichnan R.H., (1974), "On Kolmogorov's inertial-range theories", *J. Fluid Mech*., 62, 305-330
[67] Pope S.B. (2000), Turbulent Flows, Cambridge University Press, 2000
[68] Paolucci S., (1990), "Direct numerical simulation of two-dimensional turbulent natural convection in an enclosed cavity", *J. Fluid Mech*., 215, 229-262.
[69] Farhangnia M., Biringen S, Peltier L. J., (1996), "Numerical Simulation of Two-dimensional Buoyancy-driven Turbulence in a Tall Rectangular Cavity", *Int. J. Numer. Meth. Fluids*, 23(12), 1311 - 1326.
[70] Kerr R.M., (1996), "Rayleigh number scaling in numerical convection", *J. Fluid Mech*. 310, 139-179.
[71] De A.K., Eswaran V., Mishra P.K., (2017), "Scalings of heat transport and energy spectra of turbulent Rayleigh-Bénard convection in a large-aspect-ratio box", *Int. J. Heat Fluid Flow*, 67, 111–124.
[72] Lappa M. and Gradinscak T., (2018), "On the Oscillatory Modes of Compressible Thermal Convection in inclined differentially heated cavities", *Int. J. of Heat and Mass Transfer*, 121, 412–436.
[73] Hier Majumder C. A., Yuen D. A. and Vincent A., (2004), "Four dynamical regimes for a starting plume model", *Phys. Fluids*, 16(5), 1516-1531.
[74] Lappa M., (2011), "Some considerations about the symmetry and evolution of chaotic Rayleigh–Bénard convection: The flywheel mechanism and the "wind" of turbulence", *Comptes Rendus Mécanique*, 339, 563–572. DOI:10.1016/j.crme.2011.05.002
[75] Le Quéré P. and Behnia M., (1998), "From onset of unsteadiness to chaos in a differentially heated square cavity", *J. Fluid Mech*., 359, 81-107.
[76] Ferialdi H., Lappa M. and Haughey C., (2020), "On the Role of Thermal Boundary Conditions in Typical Problems of Buoyancy Convection: A Combined Numerical-Experimental Analysis", *Int. J. of Heat and Mass Transfer*, 159, 120012 (23 pages).
[77] Pera L. and Gebhart B., (1971), "On the stability of laminar plumes: Some numerical solutions and experiments", *Int. J. Heat Mass Transfer*, 14(7), 975-982.
[78] Desrayaud G. and Lauriat G., (1993), "Unsteady Confined Buoyant Plumes", *J. Fluid Mech*., 252 , 617-646.
[79] Cortese T. and Balachandar S., (1993), "Vortical nature of thermal plumes in turbulent convection", *Phys. Fluids* A, 5, 3226-3232.
[80] Vincent A.P. and Yuen D.A., (1999), "Plumes and waves in two-dimensional turbulent thermal convection", *Phys. Rev. E* 60(3), 2957-2963.